BIOCHEMISTRY

PI(4,5)P_2-dependent regulation of endothelial tip cell specification contributes to angiogenesis

Elizabeth M. Davies[1]†, Rajendra Gurung[1]†, Kai Qin Le[1], Katherine T. T. Roan[1], Richard P. Harvey[2,3], Geraldine M. Mitchell[4,5], Quenten Schwarz[6], Christina A. Mitchell[1]*

Dynamic positioning of endothelial tip and stalk cells, via the interplay between VEGFR2 and NOTCH signaling, is essential for angiogenesis. VEGFR2 activates PI3K, which phosphorylates PI(4,5)P_2 to PI(3,4,5)P_3, activating AKT; however, PI3K/AKT does not direct tip cell specification. We report that PI(4,5)P_2 hydrolysis by the phosphoinositide-5-phosphatase, INPP5K, contributes to angiogenesis. INPP5K ablation disrupted tip cell specification and impaired embryonic angiogenesis associated with enhanced DLL4/NOTCH signaling. INPP5K degraded a pool of PI(4,5)P_2 generated by PIP5K1C phosphorylation of PI(4)P in endothelial cells. INPP5K ablation increased PI(4,5)P_2, thereby releasing β-catenin from the plasma membrane, and concurrently increased PI(3,4,5)P_3-dependent AKT activation, conditions that licensed *DLL4*/*NOTCH* transcription. Suppression of PI(4,5)P_2 in *INPP5K*-siRNA cells by *PIP5K1C*-siRNA, restored β-catenin membrane localization and normalized AKT signaling. Pharmacological NOTCH or AKT inhibition in vivo or genetic β-catenin attenuation rescued angiogenesis defects in INPP5K-null mice. Therefore, PI(4,5)P_2 is critical for β-catenin/DLL4/NOTCH signaling, which governs tip cell specification during angiogenesis.

INTRODUCTION

Regulation of angiogenesis is fundamental to the establishment of a functional vasculature, which is essential for embryonic development, postnatal inflammatory responses, and tissue regeneration (*1*). Dysregulated angiogenesis leads to neovascularization, which can promote or exacerbate diabetic retinopathy, age-related macular degeneration, and cancer growth. In response to tissue-derived proangiogenic signals, endothelial cells (ECs) develop a specialized morphology comprising two distinct cell types, tip or stalk cells. Tip cells extend multiple filopodia, migrate toward a proangiogenic gradient, and establish connections between neighboring tip cells to develop integrated vessels (*2*). Nonmigratory stalk cells proliferate at the base of the sprouting vessel to form the vascular lumen and establish adherent and tight junctions that increase vessel stability. Tip/stalk cell specification requires the coordination of vascular endothelial growth factor receptor 2 (VEGFR2) and NOTCH signaling. VEGFR2 signaling promotes expression of the NOTCH ligand delta-like 4 (DLL4) in tip cells, which, in turn, activates NOTCH signaling in adjacent stalk cells to laterally suppress tip cell identity. Tip/stalk cell fates are interchangeable and dependent on VEGFR2/DLL4/NOTCH feedback mechanisms (*3*).

Many of the biological activities of VEGF in ECs require the activation of the phosphoinositide 3-kinase (PI3K)/AKT signaling cascade. VEGF-A binding to VEGFR2 activates class I PI3K, which transiently phosphorylates phosphatidylinositol 4,5 bisphosphate [PI(4,5)P_2], generating phosphatidylinositol 3,4,5 trisphosphate [PI(3,4,5)P_3], leading to activation of many effectors including AKT (*4*). The tumor suppressor phosphatase and tensin homolog (PTEN) degrades the 3-position phosphate from PI(3,4,5)P_3 to form PI(4,5)P_2 and terminates PI3K/AKT signaling in ECs. Reduced PI3K signaling via inactivation of the PI3K class 1A p110α catalytic subunit (*5*) or enhanced PI3K/AKT signaling via depletion of *Pten* (*6*) impairs angiogenesis and causes embryonic lethality in mice. However, unanswered questions in the field converge on the role this pathway plays in tip cell specification, as inactivation of *p110*α, *Pten*, or *Akt1* neither alters tip cell identity nor modifies DLL4/NOTCH signaling during developmental angiogenesis (*5*, *7*, *8*).

Little attention has been directed at the role PI(4,5)P_2 plays in angiogenesis despite its function as an essential substrate and precursor for PI3K signaling output and also as a phosphatidylinositol signal that regulates the actin cytoskeleton and adherens junctions (*9*). PI(4,5)P_2 is generated by phosphorylation of PI(4)P by the type I phosphatidylinositol phosphate 5-kinase (PIP5K1) (*10*) and is degraded by inositol polyphosphate 5-phosphatases to PI(4)P (*11*). Genetic targeting of various PI(4,5)P_2-regulatory enzymes has revealed that increased PI(4,5)P_2 signaling contributes to vascular development (*12*–*16*); however, a direct role for PI(4,5)P_2 signaling in tip cell specification during angiogenesis remains unknown.

Inositol polyphosphate 5-phosphatases (5-ptases) comprise 10 mammalian enzymes that degrade the 5-position phosphate from PI(4,5)P_2 and/or PI(3,4,5)P_3, generating PI(4)P and PI(3,4)P_2 respectively (*11*), and thus have the potential to influence multiple signaling pathways. Mutations in the 5-ptases *INPP5E*, *OCRL*, and *INPP5K* [skeletal muscle and kidney enriched inositol polyphosphate 5-phosphatase (SKIP)] cause diverse human developmental syndromes with little functional redundancy (*17*–*21*). INPP5K removes the 5-position phosphate from the inositol group of PI(4,5)P_2 generating PI(4)P (*22*). In addition, in some studies, INPP5K is proposed to degrade PI(3,4,5)P_3 to form

[1]Cancer Program, Monash Biomedicine Discovery Institute and Department of Biochemistry and Molecular Biology, Monash University, Victoria 3800, Australia. [2]Victor Chang Cardiac Research Institute, Darlinghurst, New South Wales 2010, Australia. [3]School of Clinical Medicine and School of Biotechnology and Biomolecular Science, University of New South Wales, Kensington, New South Wales 2052, Australia. [4]O'Brien Institute Department of St Vincent's Institute and University of Melbourne, Department of Surgery, St. Vincent's Hospital, Fitzroy, Victoria 3065, Australia. [5]Health Sciences Faculty, Australian Catholic University, Fitzroy, Victoria 3065, Australia. [6]Centre for Cancer Biology, SA Pathology and University of South Australia, Adelaide, South Australia 5001, Australia.
*Corresponding author. Email: christina.mitchell@monash.edu
†These authors contributed equally to this work.

$PI(3,4)P_2$, but with lower affinity and enzyme kinetics than for $PI(4,5)P_2$ (*22*–*24*). Targeted deletion of murine *Inpp5k* is embryonic lethal for unknown reasons (*25*).

Here, using in vivo and cellular models, we identify an unanticipated role for a $PI(4,5)P_2$/β-catenin/NOTCH signaling nexus in ECs and propose that the interconversion of $PI(4,5)P_2$ to PI(4)P by INPP5K functions as a gateway that facilitates tip cell specification during developmental and postnatal angiogenesis.

RESULTS

INPP5K plays an essential EC-autonomous role in embryonic angiogenesis

To investigate the cause of embryonic lethality of *Inpp5k*-null mice (*25*), $Inpp5k^{-/-}$ mice were generated using *Cre/loxP*-mediated recombination. *Inpp5k* exon 8 was flanked by *loxP* sequences ($Inpp5k^{fl/fl}$) (fig. S1A). Crossing with a germline Cre-deleter strain (*CMV*Cre) introduced a frameshift and premature stop codon before catalytic *Inpp5k* residues (*26*). Southern blotting revealed recombination at the *Inpp5k* locus (fig. S1B), and polymerase chain reaction (PCR) demonstrated the absence of the wild-type *Inpp5k* allele in $Inpp5k^{-/-}$ embryos (fig. S1C). Loss of *Inpp5k* mRNA transcripts was observed in embryonic day 9.5 (E9.5) $Inpp5k^{-/-}$ embryos (fig. S1D). *Inpp5k* heterozygous ($Inpp5k^{+/-}$) mice were viable and fertile; however, intercrosses produced no live $Inpp5k^{-/-}$ offspring (fig. S1E), confirming that homozygous deletion of *Inpp5k* induces embryonic lethality as previously reported (*25*). However, as the cause of embryonic lethality was never established, we investigated this here. $Inpp5k^{-/-}$ embryos were growth retarded at E9.5, with variable impacts on forebrain development (Fig. 1A), and no viable embryos were generated beyond E10.5 (fig. S1E). $Inpp5k^{-/-}$ E9.5 embryo cell proliferation was equivalent to wild type, as shown by phospho–histone H3 staining (fig. S1F). Many E9.5 and E10.5 $Inpp5k^{-/-}$ embryos exhibited cranial hemorrhaging (Fig. 1A, arrows), indicative of defective vasculature. The major vessels including the dorsal aorta and cardinal veins formed normally (fig. S1G); however, the head and trunk vasculature was primitive, disorganized, and dilated, and intersomitic trunk vessel development was disrupted (Fig. 1B and fig. S1H). Impaired vascular smooth muscle cell recruitment to $Inpp5k^{-/-}$ vascular endothelium was detected (fig. S1I, left), but no defects in cardiomyocyte endocardium recruitment were observed (fig. S1I, right). $Inpp5k^{-/-}$ E10.5 hearts showed no obvious abnormalities (fig. S1I, right), and hemangioblast development and blood flow appeared normal. $Inpp5k^{-/-}$ yolk sacs (E10.5) formed large vitelline vessels, but smaller capillary vessel formation was reduced and showed defects in complex vessel branching (fig. S1J). These data suggest that the cause of $Inpp5k^{-/-}$ embryonic lethality, which has not been previously reported, is due to defective angiogenesis. However, INPP5K is not required for angioblast differentiation or formation of the initial vascular plexus via vasculogenesis.

To investigate for an EC-autonomous role for INPP5K in angiogenesis, $Inpp5k^{fl/fl}$ mice were intercrossed with *Tie2*Cre transgenic mice (*27*), allowing conditional deletion of *Inpp5k* in ECs. $Inpp5k^{fl/fl}$;*Tie2*Cre embryos were not viable beyond E10.5 (fig. S1K), reminiscent of global $Inpp5k^{-/-}$ embryos. Only one EC-specific–*Inpp5k* knockout mouse was born to term of 77, with 17 predicted by Mendelian inheritance (fig. S1K). $Inpp5k^{fl/fl}$;*Tie2*Cre embryos displayed growth retardation (Fig. 1C) and hemorrhaging at E10.5 (Fig. 1C, arrows), with dilated head and trunk vessels, and reduced capillary networks (Fig. 1D), recapitulating the $Inpp5k^{-/-}$ global deletion phenotype. Abnormal angiogenesis was also observed in $Inpp5k^{fl/fl}$;*Tie2*Cre yolk sacs (fig. S1L). These data demonstrate that INPP5K plays a nonredundant EC-autonomous role that is essential for embryonic angiogenesis. See also fig. S1.

INPP5K regulates postnatal and pathological angiogenesis

We next examined the role that INPP5K plays in postnatal and pathological angiogenesis using in vivo subcutaneous Matrigel plug assays and syngeneic tumor angiogenesis models, respectively. To circumvent the embryonic lethality of $Inpp5k^{-/-}$ or $Inpp5k^{fl/fl}$;*Tie2*Cre mice, tamoxifen-inducible EC-specific *Inpp5k* knockout mice ($Inpp5k^{i\Delta EC}$) were generated, which express tamoxifen-activated Cre recombinase via the *Cdh5* promoter [*Cdh5*(PAC)-CreERT2] (*28*). Tamoxifen was administered to 6-week-old $Inpp5k^{fl/fl}$ or $Inpp5k^{fl/fl}$;*Cdh5*(PAC)-CreERT2 mice daily for five consecutive days to generate control or endothelial-specific *Inpp5k* knockout ($Inpp5k^{i\Delta EC}$) mice, respectively. Deletion of *Inpp5k* in $Inpp5k^{i\Delta EC}$ mice was confirmed by quantitative reverse transcription PCR (qRT-PCR) of highly vascularized lung tissue (fig. S2A). Vascular infiltration into Matrigel plugs implanted into either $Inpp5k^{i\Delta EC}$ or control mice did not occur in the absence of proangiogenic factors but was observed in response to basic fibroblast growth factor (bFGF; Fig. 2A) or VEGF-A stimulation (Fig. 2B) and was significantly reduced in $Inpp5k^{i\Delta EC}$ mice compared with controls (Fig. 2, A and B), indicating that INPP5K regulates postnatal angiogenesis downstream of bFGF or VEGF-A signaling.

INPP5K has been reported to play a role in highly vascularized glioblastoma, and high INPP5K expression predicts for improved long-term survival (*29*). We therefore evaluated INPP5K contribution to tumor angiogenesis as a model of pathological angiogenesis. Growth of Lewis lung carcinoma (LLC; Fig. 2C) or B16F10 melanoma (Fig. 2D) syngeneic tumors in $Inpp5k^{i\Delta EC}$ mice was reduced compared with tumor growth in control mice. The vascular density of LLC tumors was significantly decreased in $Inpp5k^{i\Delta EC}$ mice (Fig. 2E), associated with reduced tumor cell proliferation (Fig. 2E) and increased tumor cell hypoxia (Fig. 2F). No differences were observed in collagen IV (fig. S2B) or smooth muscle actin (SMA) recruitment (fig. S2C) to tumor vasculature or tumor cell apoptosis (fig. S2D). We conclude that INPP5K is necessary for tumor xenograft neovascularization, and in its absence, tumor hypoxia, impaired cell proliferation, and reduced tumor growth are observed.

INPP5K promotes tip cell specification

The INPP5K-null embryonic phenotype of impaired angiogenesis is highly reminiscent of defective tip cell identity (*2*). Accordingly, murine models of endothelial tip cell specification and migration were characterized to investigate a possible role for INPP5K in tip cell selection. At E9.5 to E10.5, tip cells from embryonic bilateral segmental trunk vessels extend filopodia and migrate from the dorsal surface, connecting with neighboring vessel tip cells, to form the paired dorsal longitudinal trunk vessels (*30*). Dorsal vascular plexus tip cell numbers were reduced in $Inpp5k^{-/-}$ embryos from E9.5, associated with decreased tip cell migration and vessel anastomoses (Fig. 3A).

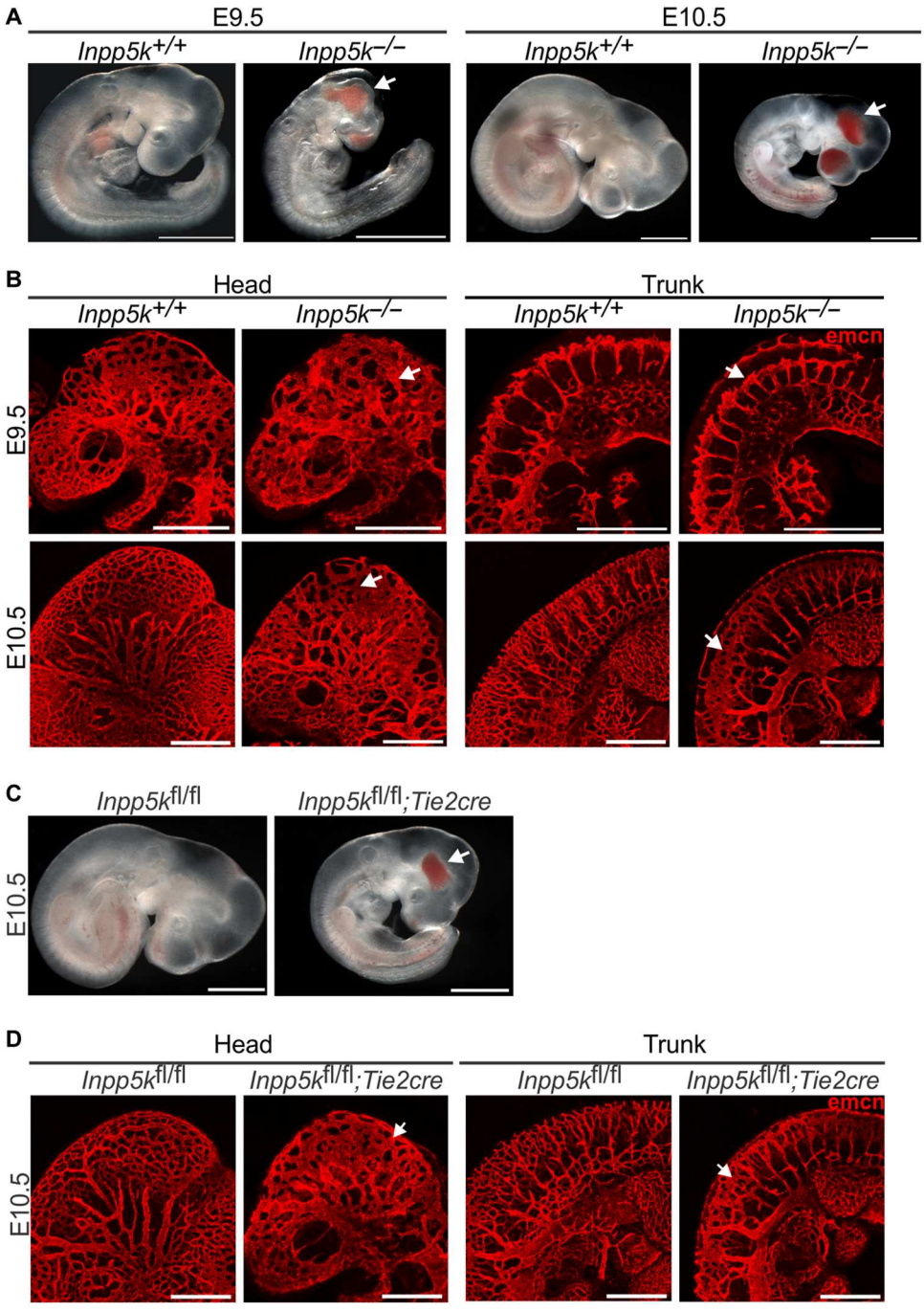

Fig. 1. INPP5K plays an essential EC-autonomous role in embryonic angiogenesis. (**A**) Bright-field microscopy images of whole-mount *Inpp5k*$^{+/+}$ or *Inpp5k*$^{-/-}$ embryos at E9.5 (left) or E10.5 (right) showing growth retardation and hemorrhage (arrows) in the head of *Inpp5k*$^{-/-}$ embryos. Scale bars, 1 mm. (**B**) Confocal microscopy images of endomucin-stained whole-mount E9.5 or E10.5 *Inpp5k*$^{+/+}$ or *Inpp5k*$^{-/-}$ embryos, depicting the vascular plexus of the head (left) or trunk (right). Arrows indicate primitive, disorganized, dilated vessels in *Inpp5k*$^{-/-}$ embryos. Scale bars, 500 μm. (**C**) Bright-field microscopy images of whole-mount *Inpp5k*$^{fl/fl}$ or *Inpp5k*$^{fl/fl}$;*Tie2*Cre embryos at E10.5 showing growth retardation and vascular hemorrhage (arrows) of *Inpp5k*$^{fl/fl}$;*Tie2*Cre embryos. Scale bars, 1 mm. (**D**) Confocal microscopy images of endomucin-stained whole-mount *Inpp5k*$^{fl/fl}$ or *Inpp5k*$^{fl/fl}$;*Tie2*Cre embryos, showing the vascular plexus of the head (left) or trunk (right). Arrows show dilated vessels and reduced capillary networks in *Inpp5k*$^{fl/fl}$;*Tie2*Cre embryos. Scale bars, 500 μm. See also fig. S1.

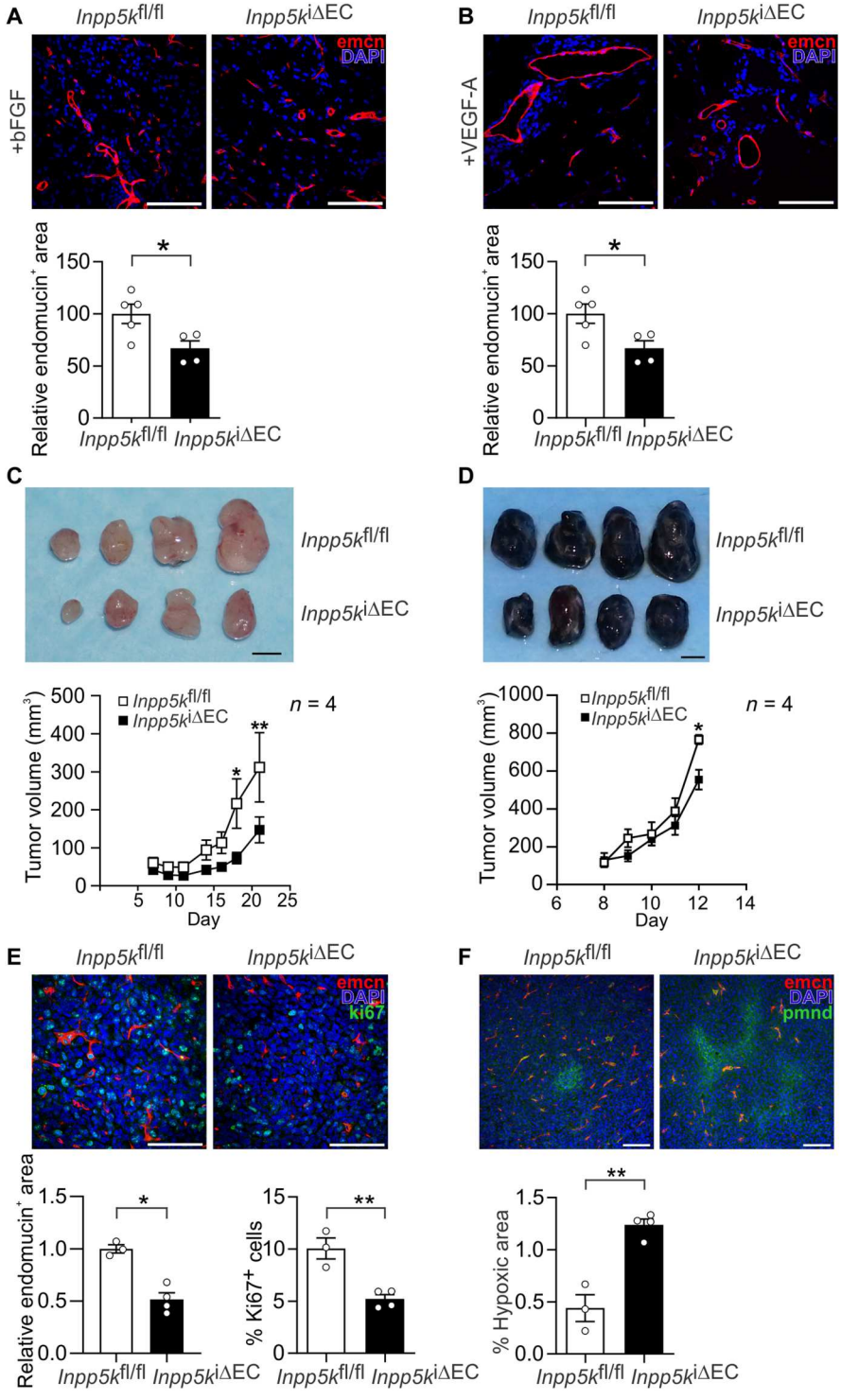

Fig. 2. INPP5K regulates postnatal and pathological angiogenesis. (**A**) Confocal images of Matrigel (500 ng of bFGF) vascular infiltration of mice 14 days after injection. Endomucin, red; DAPI, blue. Scale bars, 100 μm. Graph: Endomucin area/relative to control mice. *Inpp5k*$^{fl/fl}$, $n = 5$; *Inpp5k*$^{i\Delta EC}$, $n = 4$ mice. Means were compared by Student's *t* test, unpaired data. *$P < 0.05$. Vascularization is decreased in *Inpp5k*$^{i\Delta EC}$ mice. (**B**) Confocal images showing Matrigel (250 ng of VEGF-A) vascular infiltration from mice, 14 days after injection. Scale bars, 100 μm. Graph: Endomucin area relative to control mice ± SEM: *Inpp5k*$^{fl/fl}$, $n = 5$; *Inpp5k*$^{i\Delta EC}$, $n = 4$ mice. Means were compared by Student's *t* test, unpaired data. *$P < 0.05$. Vascularization is decreased in *Inpp5k*$^{i\Delta EC}$ mice. (**C**) Bright-field images of LLC syngeneic tumors, 25 days after transplantation of *Inpp5k*$^{fl/fl}$ or *Inpp5k*$^{i\Delta EC}$ mice. Scale bar, 5 mm. Graph: Mean tumor volumes (mm^3) ± SEM; four mice per genotype. Means were compared by Student's *t* test, unpaired data. *$P < 0.05$ and **$P < 0.01$. Tumor volumes were reduced in *Inpp5k*$^{i\Delta EC}$ mice. (**D**) Bright-field images of B16F10 melanoma syngeneic tumors from *Inpp5k*$^{fl/fl}$ or *Inpp5k*$^{i\Delta EC}$ mice 12 days after transplantation. Scale bar, 5 mm. Graph: Mean tumor volumes (mm^3) ± SEM; four mice per genotype. Means were compared by Student's *t* test, unpaired data. *$P < 0.05$. Tumor volumes are decreased in *Inpp5k*$^{i\Delta EC}$ mice. (**E**) Confocal images of LLC tumor sections at 25 days, stained for endomucin (red), Ki67 (green), and DAPI (blue). Scale bars, 50 μm. Graphs: Percent tumor vascularization area; Ki67-positive cells ± SEM; *Inpp5k*$^{fl/fl}$, $n = 3$; *Inpp5k*$^{i\Delta EC}$, $n = 4$ mice. Means were compared by Student's *t* test, unpaired data. *$P < 0.05$ and **$P < 0.01$. *Inpp5k*$^{i\Delta EC}$ tumors show reduced vascularization and proliferation. (**F**) Mice given pimonidazole hydrochloride (60 mg/kg) intraperitoneally 90 min before euthanasia. Confocal images of pimonidazole-stained (green) tumor sections at 25 days. Endomucin, red; DAPI, blue. Scale bars, 100 μm. Graph: Percent hypoxic area ± SEM: *Inpp5k*$^{fl/fl}$, $n = 3$; *Inpp5k*$^{i\Delta EC}$, $n = 4$ mice. Means were compared by Student's *t* test, unpaired data. **$P < 0.01$. Tumor hypoxia increased in *Inpp5k*$^{i\Delta EC}$ mice. See also fig. S2.

We next used models of murine retinal vascular development (*31*) to further define the role that INPP5K plays in endothelial tip cell specification. Endothelial tip cells were defined in the retinal vessels as ECs located at the outermost expanding vascular front with filopodial extensions as extensively described (*32*–*37*). Two-dimensional (2D) retinal vascular patterning defects were evident in *Inpp5k*$^{i\Delta EC}$ mice from postnatal day 5 (P5) to P7, associated with suppressed vascular expansion (Fig. 3B and fig. S3A), decreased capillary branching (Fig. 3C and fig. S3B), reduced tip cell sprouting, and diminished filopodia extension (Fig. 3D). Vascular smooth muscle cell recruitment was not impaired (fig. S3C), indicating no contribution of mural cell signaling to vascular sprouting in this model. Capillary width (Fig. 3C) and EC proliferation (fig. S3D) were unaffected. Vasculature extension

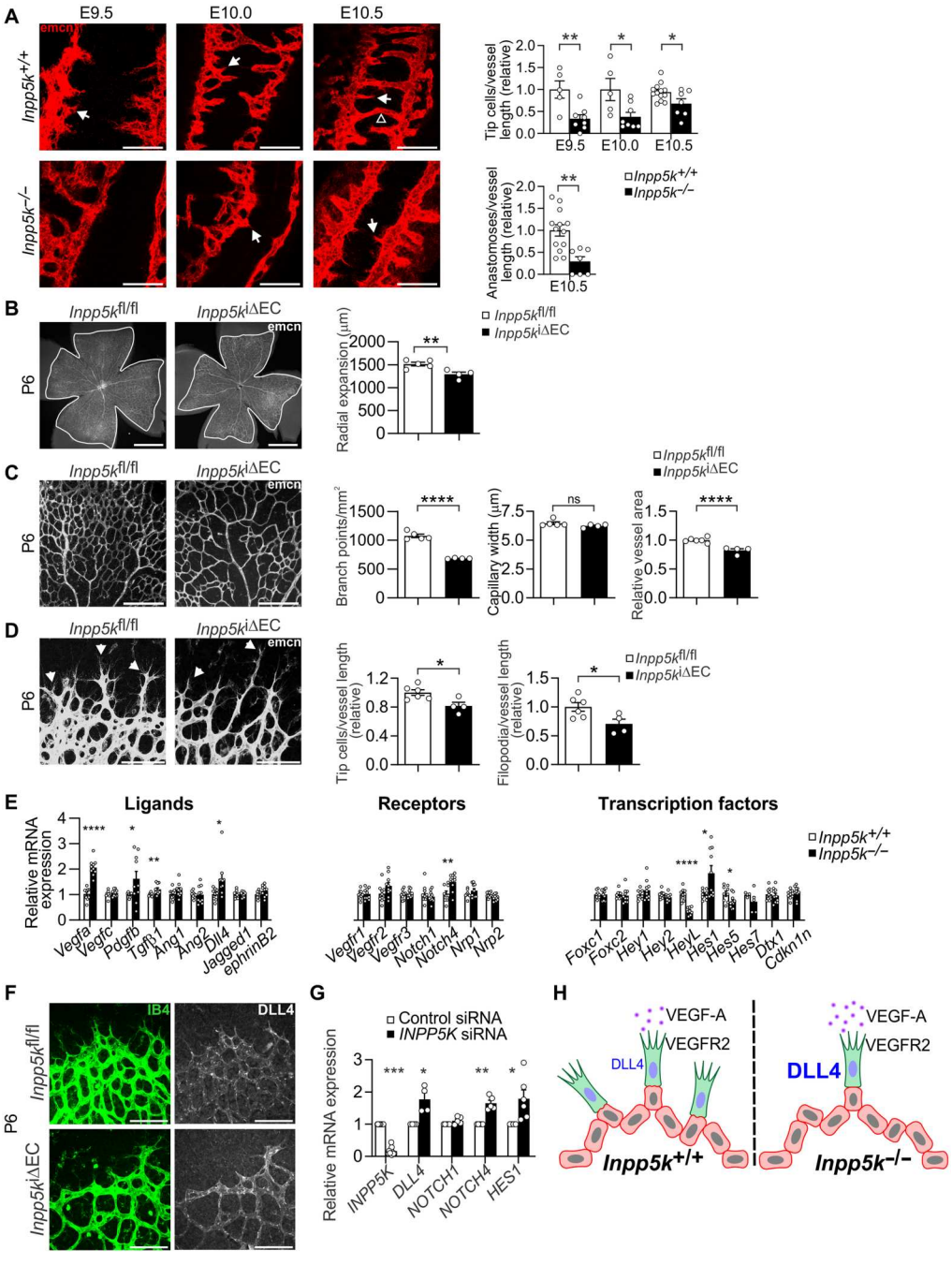

Fig. 3. INPP5K promotes tip cell specification. (**A**) Endomucin-labeled, whole-mount embryos (E9.5, E10.0, and E10.5) showing trunk dorsal longitudinal anastomotic vessels. Tip cells, arrows; vessel anastomosis, open arrowhead. Scale bars, 100 μm. Graphs: Tip cells/vessel length ± SEM: *Inpp5k*$^{+/+}$, $n = 5$ and *Inpp5k*$^{-/-}$, $n = 8$ (E9.5); *Inpp5k*$^{+/+}$, $n = 5$ and *Inpp5k*$^{-/-}$, $n = 8$ (E10.0) mice. *Inpp5k*$^{+/+}$, $n = 13$ and *Inpp5k*$^{-/-}$, $n = 7$ (E10.5) mice; anastomoses/vessel length ± SEM: *Inpp5k*$^{+/+}$, $n = 13$ and *Inpp5k*$^{-/-}$, $n = 7$ (E10.5) mice. Comparison of means, Student's *t* test, unpaired data. $^{*}P < 0.05$ and $^{**}P < 0.01$. Tip cells and vessel anastomosis are reduced in *Inpp5k*$^{-/-}$ embryos. (**B**) Endomucin-stained flat-mount P6 retina, expansion limits (outlined). Scale bars, 1 mm. Graph: Vascular expansion; $n = 4$ mice per genotype. Comparison of means, Student's *t* test, unpaired data. $^{**}P < 0.01$. Vascular expansion decreased in *Inpp5k*$^{i\Delta EC}$ retina. (**C**) Confocal images of endomucin-stained flat-mount P6 retina. Scale bars, 200 μm. Graphs: Capillary-branch points, width, vessel area ± SEM, $n = 4$ mice per genotype. Comparison of means, Student's *t* test, unpaired data. $^{****}P < 0.0001$; ns, not significant. Capillary branching and vessel area decreased in *Inpp5k*$^{i\Delta EC}$ retina. (**D**) Endomucin-stained flat-mount P6 retinal vasculature. Scale bars, 100 μm. Arrows, tip cells. Graphs: Tip cells and filopodia/relative to vessel length ± SEM, $n = 4$ mice per genotype. Comparison of means, Student's *t* test, unpaired data. $^{*}P < 0.05$. Tip cells and filopodia decreased in *Inpp5k*$^{i\Delta EC}$ retina. (**E**) mRNA expression ± SEM of $n = 9$ mice per genotype. Comparison of means, Student's *t* test, unpaired data. $^{*}P < 0.05$, $^{**}P < 0.01$, and $^{****}P < 0.0001$. INPP5K suppresses NOTCH effectors. (**F**) Confocal images of flat-mount P6 retinas stained for IB4 (green) and DLL4 (gray). Scale bars, 100 μm. DLL4 is increased in *Inpp5k*$^{i\Delta EC}$ retinal front. (**G**) NOTCH effectors in HUVECs on Matrigel [VEGF-A (50 ng/ml) for 16 hours], GAPDH control. Graph: mRNA ± SEM of four independent experiments. Comparison of means, Student's *t* test, unpaired data. $^{*}P < 0.05$, $^{**}P < 0.01$, and $^{***}P < 0.001$. NOTCH pathway activation increased by *INPP5K* loss. (**H**) Schematic: INPP5K suppresses NOTCH effectors and regulates tip cells. See also fig. S3.

into the deep retinal layers was also impaired in *Inpp5k*$^{i\Delta EC}$ mice at P9 (fig. S3E) and in the intermediate retinal layers at P15 (fig. S3F). Collectively, these data indicate that INPP5K is indispensable for endothelial tip cell specification both during embryonic development and in the postnatal retina.

To further investigate the molecular mechanisms causative of *Inpp5k*$^{-/-}$ embryonic angiogenesis defects, effectors that are known to contribute to tip cell specification were analyzed. Transcription of the VEGFR2 ligand, *Vegfa*, was increased in *Inpp5k*$^{-/-}$ embryos, as were transcripts of the EC-restricted receptor *Notch4* and its associated tip cell–enriched ligand *Dll4* (Fig. 3E). Notably, *Notch1* transcripts were not changed (Fig. 3E). Transcription of the direct NOTCH target gene, *Hes1*, was significantly increased in *Inpp5k*$^{-/-}$ embryos, indicating amplified NOTCH signaling (Fig. 3E). Transcription of *HeyL* and *Hes5* were decreased in *Inpp5k*$^{-/-}$ embryos (Fig. 3E). Transcription of *Tgfβ1* and *Pdgfb*, which enhance vessel maturation, were also increased (Fig. 3E). Platelet derived growth factor subunit B (PDGFB) is also a tip cell

marker (*2*). No change was observed in *Jagged1* (Fig. 3E), which is strongly expressed in stalk cells and is an antagonist of DLL4 (*38*). DLL4 protein was also more prominent at the retinal vascular front of *Inpp5k*$^{i\Delta EC}$ mice compared with controls (Fig. 3F). Consistent with these data, *INPP5K*-siRNA (small interfering RNA) human umbilical vein ECs (HUVECs; fig. S3, G to I) showed increased *DLL4*, *NOTCH4*, and *HES1* transcription during capillary tube formation (Fig. 3G). Collectively, these data demonstrate that INPP5K suppresses the transcriptional profile of effectors within the VEGFR2/DLL4/NOTCH signaling nexus, consistent with our observation that loss of INPP5K reduces tip cell specification (Fig. 3H).

INPP5K regulates angiogenesis by suppressing NOTCH pathway activation

In proof-of-concept studies, we used in vitro and in vivo models of INPP5K deletion to confirm that the INPP5K-null angiogenesis defects result from increased DLL4/NOTCH pathway activation. First, endothelial tube formation assays were used as an in vitro model of angiogenesis in *INPP5K*-siRNA HUVECs to complement our in vivo data, as this assay allows rapid assessment of pathway effectors through either genetic manipulation of ECs or the addition of pharmacological inhibitors or enhancers to the overlaid medium (*39*–*42*). *INPP5K*-siRNA reduced the complexity of endothelial tube formation compared with controls, with decreased average tubule length, tubule area, and interconnected tubule enclosures (fig. S4A). No change in the ratio of live to dead cells was observed in cells stained with Hoechst 33342 and propidium iodide (fig. S4B), which suggested the absence of an EC viability defect in response to ablation of INPP5K. However, upon closer examination, we observed a proportionate decrease in both Hoechst 33342 and propidium iodide staining in *INPP5K*-siRNA HUVECs compared with control cells (fig. S4B), suggesting that loss of INPP5K reduced EC viability on Matrigel. To confirm these data, we examined cell viability in HUVECs plated onto Matrigel using an alternative cell viability assay that measures adenosine triphosphate (ATP) levels as an indicator of metabolically active cells. Intracellular ATP levels were significantly decreased in *INPP5K*-siRNA cells when grown on Matrigel compared with control cells (fig. S4B), demonstrating that an EC viability defect contributes to altered tube formation. Reduced cell migration may also affect tube formation; therefore, we examined the effects of INPP5K depletion on cell migration using Transwell migration assays. *INPP5K*-siRNA HUVECs showed a 64% decrease in cell migration toward VEGF-A in Transwell migration assays (fig. S4C). Therefore, defective EC viability combined with impaired cell migration influences endothelial tube formation of *INPP5K*-siRNA HUVECs.

NOTCH or DLL4 signals were inhibited in *INPP5K*-siRNA HUVECs by pharmacological inhibition with the NOTCH γ-secretase inhibitor DAPT {*N*-[*N*-(3,5-difluorophenacetyl)-L-alanyl]-S-phenylglycine *t*-butyl ester} or the neutralizing antibody DLL4-Fc, respectively, and their effects were tested using endothelial tube formation assays or Transwell migration assays. Treatment of *INPP5K*-siRNA HUVECs with DAPT or DLL4-Fc fully restored defective endothelial tube formation (Fig. 4A) and rescued cell migration defects in *INPP5K*-siRNA HUVECs (Fig. 4B), suggesting that increased NOTCH signaling may contribute to defective angiogenesis as a consequence of INPP5K loss.

To validate these in vitro data, DAPT was intravenously administered to pregnant heterozygous *Inpp5k*$^{+/-}$ dams over 3 days (E7.5 to E9.5) and embryos extracted at E10.5 (day of expected embryonic death) and at E11.5 (1 day after expected embryonic death). Notably, four of six DAPT-treated *Inpp5k*$^{-/-}$ embryos survived beyond the expected day of embryonic death (E10.5) to E11.5, with no surviving vehicle-treated *Inpp5k*$^{-/-}$ embryos observed at this developmental stage (Fig. 4C). DAPT treatment restored embryonic growth (Fig. 4D) and normalized vascular patterning and capillary branching in E10.5 and E11.5 *Inpp5k*$^{-/-}$ embryos (Fig. 4D). In addition, restoration of E11.5 *Inpp5k*$^{-/-}$ yolk sac vasculature was also evident following DAPT treatment (Fig. 4E).

The contribution of increased NOTCH signaling to impaired tip cell specification in *Inpp5k*$^{i\Delta EC}$ retinal vasculature was also assessed. Tamoxifen was administered daily to *Inpp5k*$^{fl/fl}$;*Cdh5*(PAC)-CreERT2 neonates from P1 to P3 to generate *Inpp5k*$^{i\Delta EC}$ mice, followed by daily subcutaneous administration of DAPT from P4 to P5. Notably, DAPT treatment normalized retinal vascular expansion, vascular branching, and tip cell numbers of P7 *Inpp5k*$^{i\Delta EC}$ retinal endothelium to that observed in vehicle-treated wild-type mice (Fig. 4F). Collectively, these data show that INPP5K maintains tip cell specification, which is required for effective embryonic and postnatal angiogenesis via regulation of NOTCH signaling.

INPP5K regulates phosphoinositide conversion in ECs

To investigate the mechanisms by which INPP5K suppresses DLL4/NOTCH signaling, we began by evaluating the status of phosphoinositides that are dephosphorylated by INPP5K in the endothelium. $PI(4,5)P_2$ and $PI(3,4,5)P_3$ are the principal substrates of INPP5K, which are hydrolyzed to PI(4)P and $PI(3,4)P_2$, respectively (*22*–*24*). These studies reported that both $PI(4,5)P_2$ and $PI(3,4,5)P_3$ phosphoinositides accumulate in cells when INPP5K is depleted, but INPP5K shows a preference for $PI(4,5)P_2$ over $PI(3,4,5)P_3$ based on enzyme kinetics using purified recombinant enzyme (*22*–*24*). However, these techniques cannot visualize changes in the generation or localization of specific phosphoinositide pools in subcellular regions or within a population of polarized cells. To the best of our knowledge to date, $PI(4,5)P_2$ and $PI(3,4,5)P_3$ distribution has not been examined in ECs during angiogenesis. To this end, phosphoinositide species were examined in P6 *Inpp5k*$^{i\Delta EC}$ retinal vasculature by phosphoinositide antibody staining using well characterized antibodies (*43*–*46*). Notably, $PI(4,5)P_2$ staining was increased, and PI(4)P decreased in *Inpp5k*$^{i\Delta EC}$ retinal vasculature (Fig. 5A). $PI(3,4,5)P_3$ staining was also increased in P6 *Inpp5k*$^{i\Delta EC}$ retinal vasculature (Fig. 5A), and $PI(3,4)P_2$ was reduced (Fig. 5A), consistent with previous reports that INPP5K directs $PI(4,5)P_2$ to PI(4)P and $PI(3,4,5)P_3$ conversion to $PI(3,4)P_2$ (*22*–*24*). Similar analysis was undertaken in *INPP5K*-siRNA HUVECs using either phosphoinositide antibody staining (*43*–*46*) or recruitment of the $PI(3,4,5)P_3$ phosphoinositide biosensor green fluorescent protein (GFP)–Pleckstrin homology domain (PH)/Bruton's tyrosine kinase (Btk) or the $PI(3,4)P_2$ biosensor yellow fluorescent protein (YFP)–PH/(Tandem PH domain-containing protein (TAPP1) (*47*, *48*). *INPP5K*-siRNA HUVECs showed increased plasma membrane $PI(4,5)P_2$ in unstimulated and VEGF-stimulated cells relative to controls (fig. S5A). PI(4)P signals at the plasma membrane were decreased in *INPP5K*-siRNA HUVECs compared with controls (fig. S5B). No difference in plasma membrane $PI(3,4,5)P_3$ or $PI(3,4)P_2$ signals was observed

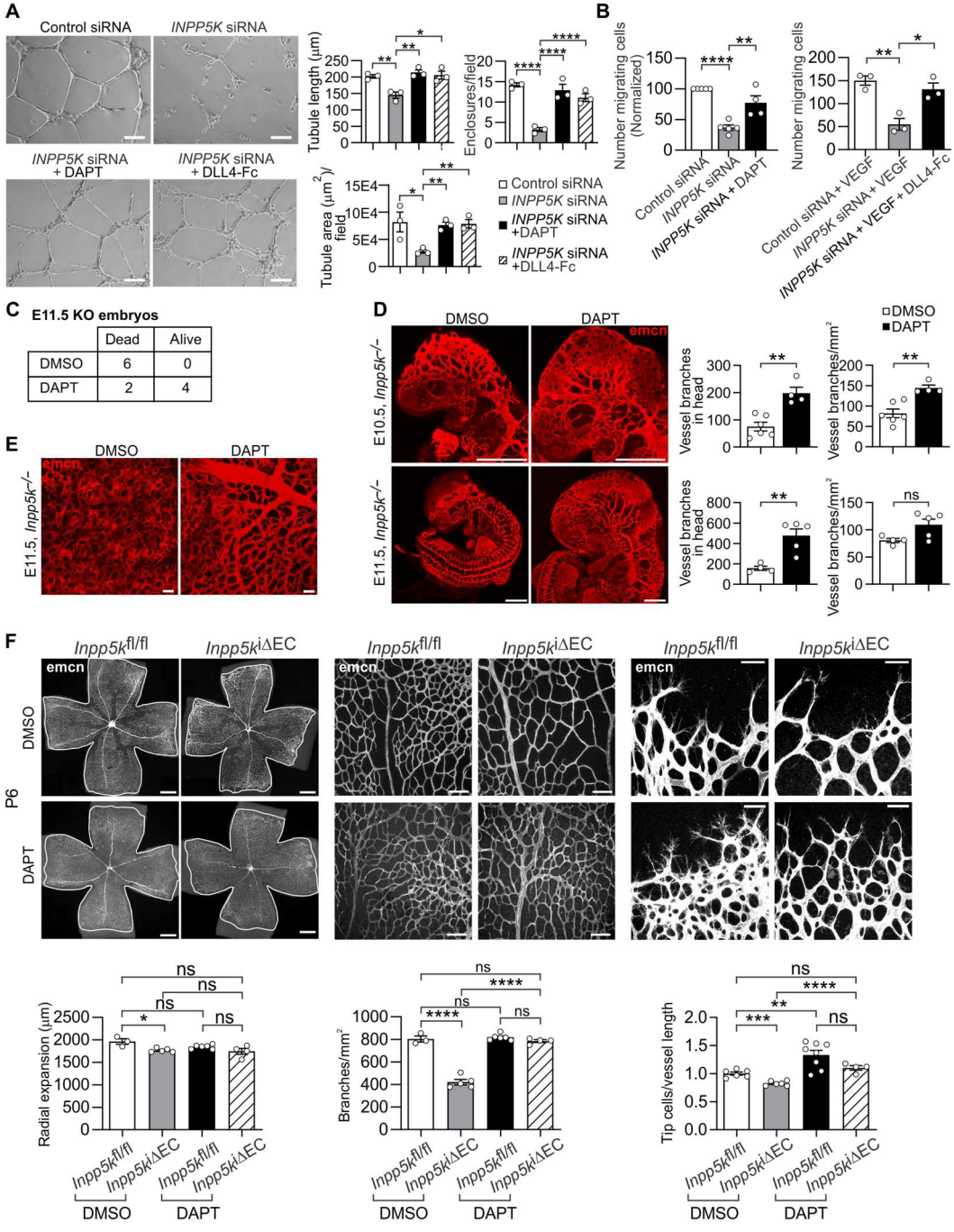

Fig. 4. INPP5K regulates angiogenesis by suppressing NOTCH pathway activation. (**A**) Bright-field images of endothelial tubes [Matrigel, 16 hours of VEGF-A (50 ng/ml) ± 5 μM DAPT, or DLL4-Fc (±5 μg/ml)]. Scale bars, 125 μm. Graphs: Tubule length, area, and interconnected tubule enclosures as means ± SEM of three independent experiments. Statistics: Analysis of variance (ANOVA) followed by Tukey's post hoc test. **P* < 0.05, ***P* < 0.01, and *****P* < 0.0001. DLL4/NOTCH inhibition rescues *INPP5K*-siRNA HUVEC tubule defects. (**B**) Transwell [VEGF-A (50 ng/ml) ± 5 μM DAPT or DLL4-Fc (±5 μg/ml)] cell migration quantified 12 independent fields. Mean cells/field ± SEM, three independent experiments. Statistics: ANOVA and Tukey's post hoc test. ***P* < 0.01 and *****P* < 0.0001. NOTCH/DLL4 inhibition restores *INPP5K*-siRNA HUVECs migration. (**C**) DAPT (50 μg/g body weight to dams), E11.5 *Inpp5k*$^{-/-}$ survival, from *Inpp5k*$^{+/-}$ mice timed mating. NOTCH inhibition extends *Inpp5k*$^{-/-}$ embryo viability. (**D**) Confocal images of endomucin-stained whole-mount E10.5 or E11.5 *Inpp5k*$^{-/-}$ embryos, DMSO-vehicle, or DAPT (50 μg/g to dams) treated. Scale bars, 500 μm. Graphs: Vessel branches/unit area in the head; *Inpp5k*$^{+/+}$, *n* = 6 and *Inpp5k*$^{-/-}$, *n* = 4 (E10.5) mice; *Inpp5k*$^{+/+}$, *n* = 5 and *Inpp5k*$^{-/-}$, *n* = 8 (E11.5) mice. Means compared by Student's *t* test, unpaired data. ***P* < 0.01. NOTCH inhibition improves *Inpp5k*$^{-/-}$ embryo angiogenesis. (**E**) Confocal images of endomucin-stained flat-mount E11.5 *Inpp5k*$^{-/-}$ yolk sacs, DMSO-vehicle, or DAPT (50 μg/g body weight to dams) treated. Scale bars, 100 μm. NOTCH inhibition improves *Inpp5k*$^{-/-}$ embryo–yolk sac angiogenesis. (**F**) Confocal images of endomucin-stained flat-mount P6 retina from mice treated with 200 μg of DAPT or DMSO-vehicle. Radial-vascular expansion (left; scale bars, 500 μm), capillary-branch points (middle; scale bars, 100 μm), vascular-front (right; scale bars, 50 μm). Graphs: Mean radial vascular expansion; branches/mm^2; tip cells ± SEM. Statistics: ANOVA and Tukey's post hoc test. **P* < 0.05, ***P* < 0.01, ****P* < 0.001, and *****P* < 0.0001; NOTCH inhibition restores radial expansion, branching, and tip cells in *Inpp5k*$^{i\Delta EC}$ mice. See also fig. S4.

in control or *INPP5K*-siRNA HUVECs that were serum-starved (fig. S5, C and D). In response to VEGF-A stimulation, *INPP5K*-siRNA HUVECs showed significantly increased plasma membrane PI(3,4,5)P_3 compared with controls, associated with decreased PI(3,4)P_2 (fig. S5, C and D). In validation studies, no change in PI(3)P recruitment was detected in *INPP5K*-siRNA HUVECs compared to controls (fig. S5E). Therefore, INPP5K is essential for maintaining PI(4,5)P_2 and PI(3,4,5)P_3 and their conversion to PI(4)P and PI(3,4)P_2, respectively, in ECs during angiogenesis (Fig. 5B).

INPP5K and PIP5K1C play opposing roles in PI(4,5)P_2 regulation during endothelial tube formation

To further investigate the role that PI(4,5)P_2 plays in angiogenesis, we examined both its respective synthesis and hydrolysis in ECs by the PI(4)P 5-kinase PIP5K1 and PI(4,5)P_2 5-phosphatase INPP5K.

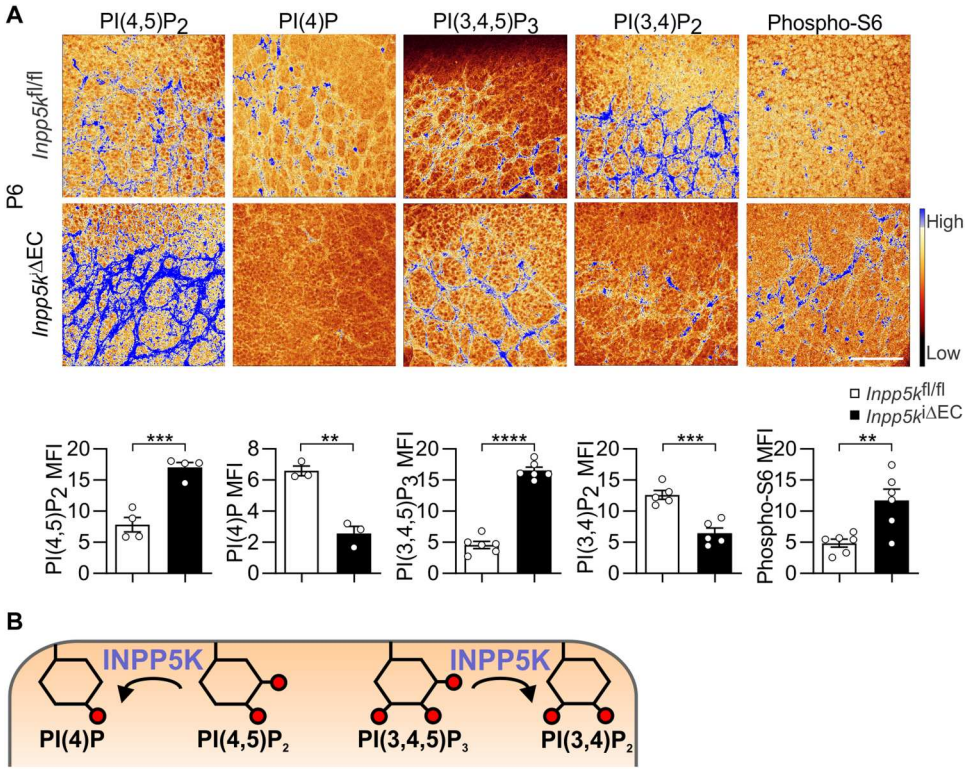

Fig. 5. INPP5K regulates phosphoinositide conversion in ECs. (**A**) Confocal microscopy images of flat-mount P6 *Inpp5k*$^{fl/fl}$ or *Inpp5k*$^{i\Delta EC}$ retina stained with antibodies to PI(4,5)P_2, PI(4)P, PI(3,4,5)P_3, PI(3,4)P_2, or phospho-S6. Scale bar, 80 μm. Phosphoinositide staining displayed in glow-over mode; high-intensity staining is white-blue, and low-intensity staining is black-red. Graphs represent mean fluorescence intensity ± SEM of phosphoinositide or phospho-S6 relative to background retinal staining. *Inpp5k*$^{fl/fl}$, $n = 4$; *Inpp5k*$^{i\Delta EC}$, $n = 4$ [PI(4,5)P_2]; *Inpp5k*$^{fl/fl}$, $n = 3$; *Inpp5k*$^{i\Delta EC}$, $n = 3$ [PI(4)P]; *Inpp5k*$^{fl/fl}$, $n = 6$; *Inpp5k*$^{i\Delta EC}$, $n = 6$ [PI(3,4,5)P_3]; *Inpp5k*$^{fl/fl}$, $n = 5$; *Inpp5k*$^{i\Delta EC}$, $n = 5$ [PI(3,4)P_2]; *Inpp5k*$^{fl/fl}$, $n = 6$; *Inpp5k*$^{i\Delta EC}$, $n = 6$ (phospho-S6). Comparison between the means was assessed using Student's *t* test for unpaired data. $^{**}P < 0.01$, $^{***}P < 0.001$, and $^{****}P < 0.0001$. PI(4,5)P_2 and PI(3,4,5)P_3 signals are elevated in *Inpp5k*$^{i\Delta EC}$ retinal vasculature. (**B**) Schematic showing phosphoinositide interconversion mediated by INPP5K in ECs. INPP5K hydrolyzes both PI(4,5)P_2 and PI(3,4,5)P_3. See also fig. S5.

PIP5K1 isoforms (PIP5K1A, PIP5K1B, and PIP5K1C) generate PI(4,5)P_2 by phosphorylation of PI(4)P (*10*). The relative expression of each *PIP5K1* isoform in parental HUVECs was assessed by droplet digital PCR analysis of mRNA, revealing that *PIP5K1A* and *PIP5K1C* are the predominant isoforms in ECs, with *PIP5K1B* transcripts below the limit of detection (fig. S6A). Capillary tube formation assays were used here as an in vitro model (*39*–*42*) to assess the contribution of PIP5K1A and PIP5K1C isoforms to angiogenesis. *PIP5K1A* or *PIP5K1C* were depleted by siRNA in HUVECs with ~70 to 80% knockdown efficiency (fig. S6B). Notably, *PIP5K1C*-siRNA HUVECs displayed reduced average tubule length, tubule area and interconnected tubule formation compared with controls. However, *PIP5K1A* depletion did not impair tubule formation (fig. S6C), indicating that PIP5K1C-mediated and not PIP5K1A-mediated generation of PI(4,5)P_2 contributes to EC tube formation.

The relative roles of INPP5K and PIP5K1C in EC tube formation were further investigated by transfecting HUVECs with nontargeting control, *INPP5K* or *PIP5K1C* siRNA, or with combined *INPP5K* and *PIP5K1C* siRNA oligonucleotides. Greater than 80% knockdown of *INPP5K* or *PIP5K1C* was achieved with either single or concomitant transfection of siRNAs (fig. S6, D and E). PI(4,5)P_2 staining was increased in *INPP5K*-siRNA HUVECs grown in serum, consistent with reduced PI(4,5)P_2 hydrolysis and, in contrast, was decreased in *PIP5K1C*-siRNA cells, consistent with its reduced synthesis (Fig. 6A). HUVECs with concomitant depletion of *INPP5K* and *PIP5K1C* exhibited PI(4,5)P_2 staining similar to controls (Fig. 6A). PI(4)P was decreased in *INPP5K*-siRNA HUVECs and increased in *PIP5K1C*-siRNA cells, with correction following concurrent knockdown of *INPP5K* and *PIP5K1C* (Fig. 6A). Thus, INPP5K can access and degrade the pool of PI(4,5)P_2 generated by PIP5K1C phosphorylation of PI(4)P in ECs.

The capacity of HUVECs to form capillary-like tubules was undertaken to assess the contribution of INPP5K and PIP5K1C to PI(4,5)P_2-dependent angiogenesis. Both *INPP5K*-siRNA, which increased PI(4,5)P_2, and *PIP5K1C*-siRNA, which decreased PI(4,5)P_2, reduced the complexity of endothelial tube formation compared with controls, with decreased average tubule length, tubule area, and interconnected tubule enclosures (Fig. 6B). Concurrent *INPP5K* and *PIP5K1C* silencing significantly improved but did not completely restore EC tubule defects observed with either *INPP5K* or *PIP5K1C* knockdown (Fig. 6B). Therefore, regulation of PI(4,5)P_2 by both the PI(4)P 5-kinase PIP5K1C and the PI(4,5)P_2 5-phosphatase INPP5K is required during EC tube formation.

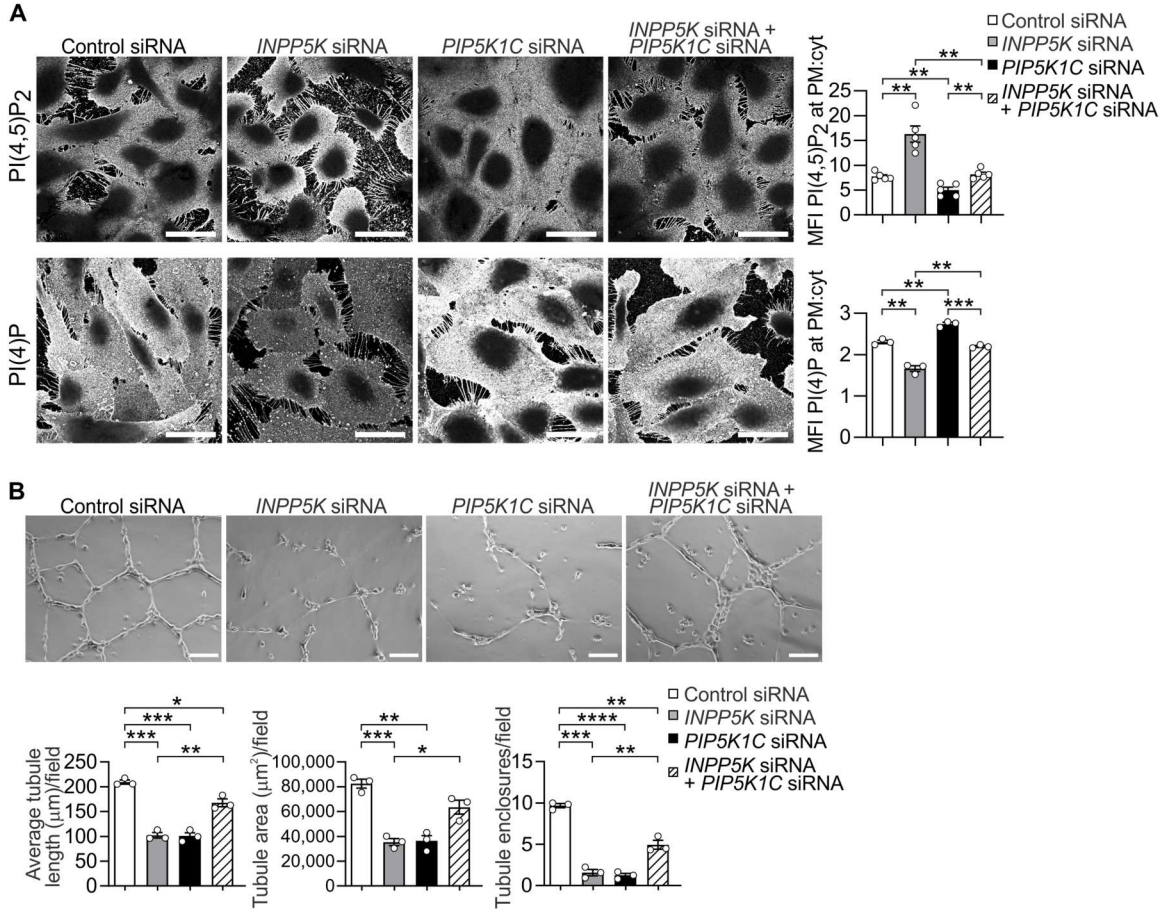

Fig. 6. INPP5K and PIP5K1C play opposing roles in PI(4,5)P_2 regulation during endothelial tube formation. (**A**) PI(4,5)P_2 or PI(4)P accumulation at the plasma membrane was assessed by indirect immunofluorescence in *PIP5K1C*, *INPP5K*, or *PIP5K1C* + *INPP5K*-siRNA HUVECs or controls grown in a confluent monolayer using antibodies to PI(4,5)P_2 or PI(4)P, respectively. Fluorescence intensity of PI(4,5)P_2/PI(4)P at the plasma membrane relative to the cytosol in single *z*-plane images is expressed as mean ± SEM. More than 150 cells were analyzed per treatment over five independent transfections for PI(4,5)P_2 measurements. More than 100 cells were analyzed per treatment over three independent transfections for PI(4)P measurements. Statistical analysis was performed with one-way ANOVA followed by Tukey's post hoc test. $^{**}P < 0.01$ and $^{***}P < 0.001$. Scale bars, 50 μM. Increased PI(4,5)P_2 in *INPP5K*-siRNA HUVECs is rescued with concomitant knockdown of *INPP5K* and *PIP5K1C*. (**B**) Bright-field microscopy images of *INPP5K*-siRNA or *PIP5K1C*-siRNA HUVEC endothelial tube formation on GFR Matrigel at 16 hours in medium containing VEGF-A (50 ng/ml). Scale bars, 125 μm. Graphs depict average tubule length, tubule area, and number of interconnected tubule enclosures as means ± SEM of three independent experiments. Statistical analysis was performed with one-way ANOVA followed by Tukey's post hoc test. $^{*}P < 0.05$, $^{**}P < 0.01$, $^{***}P < 0.001$, and $^{****}P < 0.0001$. *INPP5K*-siRNA and *PIP5K1C*-siRNA HUVECs show disrupted tubule formation that is rescued with concurrent knockdown of both *INPP5K* and *PIP5K1C*. See also fig. S6.

PI(4,5)P_2 contributes to maximal PI3K/AKT signaling in ECs

Inpp5k$^{i\Delta EC}$ retinal vasculature exhibited evidence of AKT pathway activation with increased phosphorylation of the ribosomal protein S6 (S6) (Fig. 5A), consistent with the observed increased PI(3,4,5)P_3, and despite reduced PI(3,4)P_2, which is required for full activation of AKT (*49*). AKT phosphorylation at Thr^{308} and Ser^{473} was also increased in *INPP5K*-siRNA HUVECs after 10 min of VEGF-A stimulation (Fig. 7A), which was dependent on class IA PI3K, as shown by use of the p110α inhibitor BYL719, which suppressed the increased AKT activation in *INPP5K*-siRNA HUVECs (fig. S7A). No change in extracellular signal–regulated kinase 1/2 (ERK1/2) activation was observed (Fig. 5A). The downstream target of AKT, glycogen synthase kinase 3β (GSK3β), also showed increased phosphorylation in *INPP5K*-siRNA HUVECs (Fig. 7A). Increased forkhead box protein O1 (FOXO1) phosphorylation was observed even in unstimulated *INPP5K*-siRNA cells (Fig. 7A) and consistent with this, FOXO1 protein was significantly reduced to 30 to 50% of control levels (Fig. 7A), indicative of posttranscriptional FOXO1 hyperphosphorylation and its ubiquitin-mediated degradation (*50*).

Constitutive or endothelial deletion of murine *Foxo1* is embryonic lethal because of impaired angiogenesis (*51*–*53*); however, heterozygous deletion of *Foxo1* has no consequence on vascular development or embryonic viability (*51*, *52*). *Foxo1* deletion in the postnatal retina inhibits vascular expansion (*54*); however, this is associated with conflicting effects on tip cell specification (*54*–*56*) despite evidence in cell culture models that FOXO1 suppresses *DLL4* transcription (*55*). Notably, *Foxo1* deletion increases EC proliferation and vascular hyperplasia (*54*, *56*) caused by unrestrained endothelial metabolic activity (*54*). Here, deletion of *Inpp5k* caused vascular hypoplasia and did not alter EC proliferation in murine models of embryonic or postnatal vascular development. In

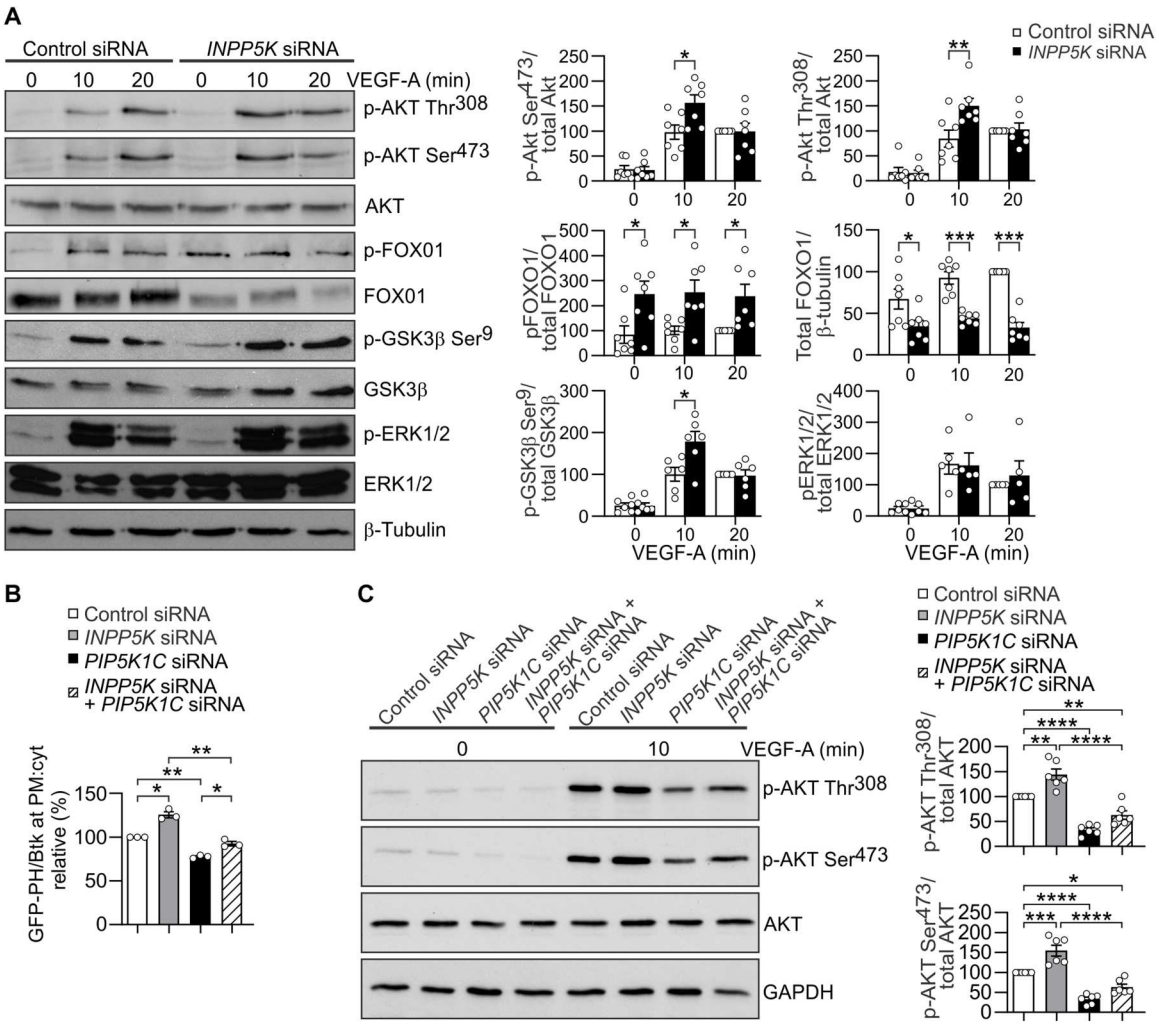

Fig. 7. PI(4,5)P_2 contributes to maximal PI3K/AKT signaling in ECs. (**A**) Control or *INPP5K*-siRNA HUVECs were serum-starved for 5 hours and then stimulated with VEGF-A (100 ng/ml) for 10 or 20 min. Soluble fractions were immunoblotted with the indicated antibodies. Graphs depict quantification of AKT pathway activation by densitometry of phosphorylated protein relative to total protein, as means ± SEM, relative to siRNA control cells at 20 min of VEGF-A. Comparison between the means was assessed using Student's *t* test for unpaired data. **P* < 0.05, ***P* < 0.01, and ****P* < 0.001. AKT pathway activation is enhanced in *INPP5K*-siRNA HUVECs. (**B**) PI(3,4,5)P_3 accumulation at the plasma membrane assessed by indirect immunofluorescence of GFP-PH/Btk. Cells were serum-starved for 5 hours and stimulated with VEGF-A (100 ng/ml) for 10 min. Fluorescence intensity of GFP-PH/Btk at the plasma membrane relative to the cytosol in single *z*-plane images is expressed as mean ± SEM. More than 100 cells were analyzed per treatment for three independent transfections. Statistical analysis by ANOVA, followed by Tukey's post hoc test. **P* < 0.05 and ***P* < 0.01. Increased PI(3,4,5)P_3 in *INPP5K*-siRNA HUVECs is rescued with concomitant knockdown of *INPP5K* and *PIP5K1C*. (**C**) *INPP5K*-siRNA and *PIP5K1C*-siRNA HUVECs were serum-starved for 5 hours and then stimulated with VEGF-A (100 ng/ml) for 10 min. Soluble fractions were subjected to immunoblot analysis with the indicated antibodies. Graphs depict quantification of AKT pathway activation determined by densitometry of phosphorylated AKT, relative to total AKT protein, expressed as means ± SEM of six independent experiments and standardized to siRNA control cells at 10 min of VEGF-A stimulation. Statistical analysis by ANOVA followed by Tukey's post hoc test. **P* < 0.05, ***P* < 0.01, ****P* < 0.001, and *****P* < 0.0001. Concurrent knockdown of both *INPP5K* and *PIP5K1C* partially restores enhanced AKT phosphorylation of *INPP5K* HUVECs. See also fig. S7.

addition, as we show here, *INPP5K*-siRNA HUVECs showed reduced cell viability (fig. S4, B and C). Whether the observed decrease in FOXO1 protein in *INPP5K*-siRNA HUVECs is sufficient to influence the murine *Inpp5k* knockout phenotype or whether depletion of INPP5K leads to metabolic uncoupling remains a subject of further investigation. Here, given the inconsistencies between the phenotype of *Inpp5k* versus *Foxo1* knockout mice, we explored alternative mechanisms to FOXO1 by which INPP5K may contribute to angiogenesis.

The class I PI3K substrate PI(4,5)P_2 is present in excess compared with PI(3,4,5)P_3 on the inner leaflet of the plasma membrane (*9*); however, recent studies indicate that PI(3,4,5)P_3 generation may require localized de novo synthesis of PI(4,5)P_2 via the cooperation of multiple phosphoinositide kinases (*57*, *58*), and thereby, PI(4,5)P_2 as a substrate may be limiting for PI(3,4,5)P_3 synthesis. This is facilitated by the scaffold protein IQ motif–containing guanosine triphosphatase–activating protein 1 that regulates the spatiotemporal assembly of a multi-enzyme complex in response to receptor activation, which encompasses the entire enzymatic

complement of the PI3K/AKT signaling pathway, including PI4KIIIα, PIP5KIα, class I PI3K, PDK1, and AKT (*57*). This complex sequentially generates PI(4)P, PI(4,5)P_2 and PI(3,4,5)P_3 from phosphatidylinositol, which then activates the PI(3,4,5)P_3 effector proteins PDK1 and AKT. Thus, PI(4,5)P_2 synthesis may be tightly coupled to PI(3,4,5)P_3 generation and AKT activation in some cell types. Here, we explored the interconversion of PI(4,5)P_2 and PI(4)P by INPP5K and PIP5K1C and its impact on PI3K/AKT signaling in ECs. VEGF-stimulated PI(3,4,5)P_3 was assessed by GFP-PH/Btk recruitment to the plasma membrane in *INPP5K*- and *PIP5K1C*-siRNA HUVECs. Plasma membrane PI(3,4,5)P_3 was increased in *INPP5K*-siRNA HUVECs compared with controls, while *PIP5K1C* knockdown decreased PI(3,4,5)P_3 (Fig. 7B and fig. S7B). Concomitant knockdown of the 5-kinase and 5-phosphatase restored PI(3,4,5)P_3 to control levels (Fig. 7B and fig. S7B). In accordance with these data, phosphorylation of AKT was increased in *INPP5K*-siRNA HUVECs and decreased in *PIP5K1C*-siRNA HUVECs (Fig. 7C). Concurrent knockdown of *INPP5K* and *PIP5K1C* partially restored AKT phosphorylation to control levels (Fig. 7C). These studies suggest that INPP5K gates the pool of PI(4,5)P_2 that fluxes into PI3K/AKT signaling in ECs.

We also investigated whether INPP5K regulation of capillary tubule formation is dependent on PI3K/AKT signaling. Pan-PI3K inhibition (LY294002) abrogated interconnected tube formation in control cells and caused further degradation of tubules in *INPP5K*-siRNA cells (Fig. 8A). Inhibition of class IA PI3K with the p110α inhibitor BYL719 also reduced tube formation in both control and *INPP5K*-siRNA HUVECs (fig. S8), indicating that p110α activation is necessary for effective endothelial tube formation and is consistent with the unconditional requirement of p110α-generated PI(3,4,5)P_3 for angiogenesis (*5*). AKT inhibition (MK2206 or AKT inhibitor X) prevented tube formation in control cells and fully rescued defective tube formation in *INPP5K*-siRNA ECs (Fig. 8A). AKT inhibition also restored the increased *DLL4* and *HES1* expression in *INPP5K*-siRNA HUVECs to control levels (Fig. 8B). These data are in accordance with a model whereby INPP5K functions downstream of PI3K to hydrolyse PI(3,4,5)P_3 but acts upstream of AKT activation, which it regulates through hydrolysis of both PI(3,4,5)P_3 and PI(4,5)P_2 signals. Our interpretation of these data is that in the context of endothelial INPP5K ablation and high PI(4,5)P_2 signals, AKT activation is increased and may contribute to *NOTCH* effector transcription. This is likely a consequence of increased PI(4,5)P_2 availability for PI3K generation of PI(3,4,5)P_3, plus reduced PI(3,4,5)P_3 hydrolysis (Fig. 8C). These data are notable considering that inactivation of *Akt1* alone does not regulate DLL4/NOTCH signaling during developmental angiogenesis (*8*).

We also explored whether AKT regulation by INPP5K plays a key role in tip cell specification in *Inpp5k*$^{i\Delta EC}$ retinal vasculature. To this end, the pharmacological AKT inhibitor MK2206 was administered daily to *Inpp5k*$^{i\Delta EC}$ and wild-type neonatal mice at P4 and P5 and the retinal vasculature examined by immunofluorescence analysis at P7. MK2206 treatment decreased retinal vascular expansion in wild-type mice but had no effect on retinal vascular expansion in *Inpp5k*$^{i\Delta EC}$ neonates (Fig. 8D), a likely consequence of the known growth suppressive effects of AKT inhibition (*59*). Notably, AKT inhibition significantly increased the numbers of tip cells in *Inpp5k*$^{i\Delta EC}$ retinal vessels compared with vehicle-treated *Inpp5k*$^{i\Delta EC}$ neonates, although not to the levels observed in vehicle-treated wild-type mice (Fig. 8E). AKT inhibition had no effect on tip cell numbers at the retinal vascular front of control mice (Fig. 8E). These data provide evidence to support a model whereby increased AKT activation contributes to the impaired angiogenesis phenotype of INPP5K-null mice.

INPP5K regulates β-catenin transcriptional activity

DLL4 expression in ECs is intimately associated with angiogenic sprouting via tip cell specification; however, the precise mechanism(s) governing its transcriptional regulation are still emerging. Several transcription factors, including the Wnt signaling effector β-catenin, SRY-box transcription factor F (SOXF), E26 transformation-specific (ETS), FOXO1, and forkhead box protein C (FOXC), contribute to DLL4 expression in ECs (*55*, *60*–*63*). The FOXC1/2 transcription factors predominantly govern arteriovenous identity during angiogenesis via direct transcription of *DLL4* (*61*); however, arteriovenous malformations are not a feature of *Inpp5k*$^{-/-}$ mice. SOXF transcription factors also directly regulate *DLL4* transcription, but they primarily direct arterial specification rather than tip cell selection (*62*). A VEGF/mitogen-activated protein kinase (MAPK)/ERK/ETS-related gene (ERG)/p300 transcriptional pathway is also required for induction of *DLL4* in ECs during angiogenesis (*63*); however, activation of MAPK/ERK signaling was not affected here by INPP5K.

β-Catenin has a known role in *DLL4* transcription and is a component of endothelial adherens junctions, which directly interacts with vascular endothelial cadherin (VE-cadherin) (*64*). Once free from adherens junctions, β-catenin can translocate to the nucleus to promote gene transcription via engagement with DNA-bound T cell factor/lymphoid enhancer factor (TCF/LEF) transcription factors. PIP5K1C interacts directly with β-catenin, and ectopic expression of kinase-active PIP5K1C in epithelial cells enhances β-catenin nuclear localization and transcriptional activity (*65*), indicating that PI(4,5)P_2 generation via PIP5K1C may contribute to β-catenin–mediated transcriptional activation. PI3K/AKT signaling induces formation of β-catenin/NOTCH intracellular domain (NICD) transcriptional complexes in cell-based experimental models, which enhance endothelial NOTCH pathway activation (*66*–*68*), yet the mechanisms governing this pathway are still emerging. In contrast, evidence from in vivo PI3K/AKT loss-of-function murine models suggests that this signaling pathway does not directly regulate DLL4 expression or tip cell identity during developmental angiogenesis (*5*, *8*).

Here, we explored whether PI(4,5)P_2 and/or PI3K/AKT independently or cooperatively regulate β-catenin transcriptional activity, which, in turn, contributes to increased *Dll4* expression in *Inpp5k*$^{-/-}$ ECs. Notably, deletion of β-catenin is embryonic lethal because of defective angiogenesis (*69*), and impaired endothelial β-catenin signaling reduces postnatal retinal and brain angiogenesis, sprouting, and tip cell formation (*70*). Conversely, endothelial β-catenin gain-of-function mutants are also embryonic lethal, resulting from impaired angiogenesis, associated with enhanced *Dll4* transcription through TCF transcriptional activation (*60*). We took several approaches to determine whether INPP5K regulates DLL4 expression via β-catenin. First, we examined β-catenin transcriptional activation in cells expressing the β-catenin TCF/LEF luciferase reporter plasmid p*TOP*Flash-Luc. Using multiple methods, transfection of p*TOP*Flash-Luc in *INPP5K*-siRNA HUVECs was unsuccessful in our hands; however, we effectively transfected the

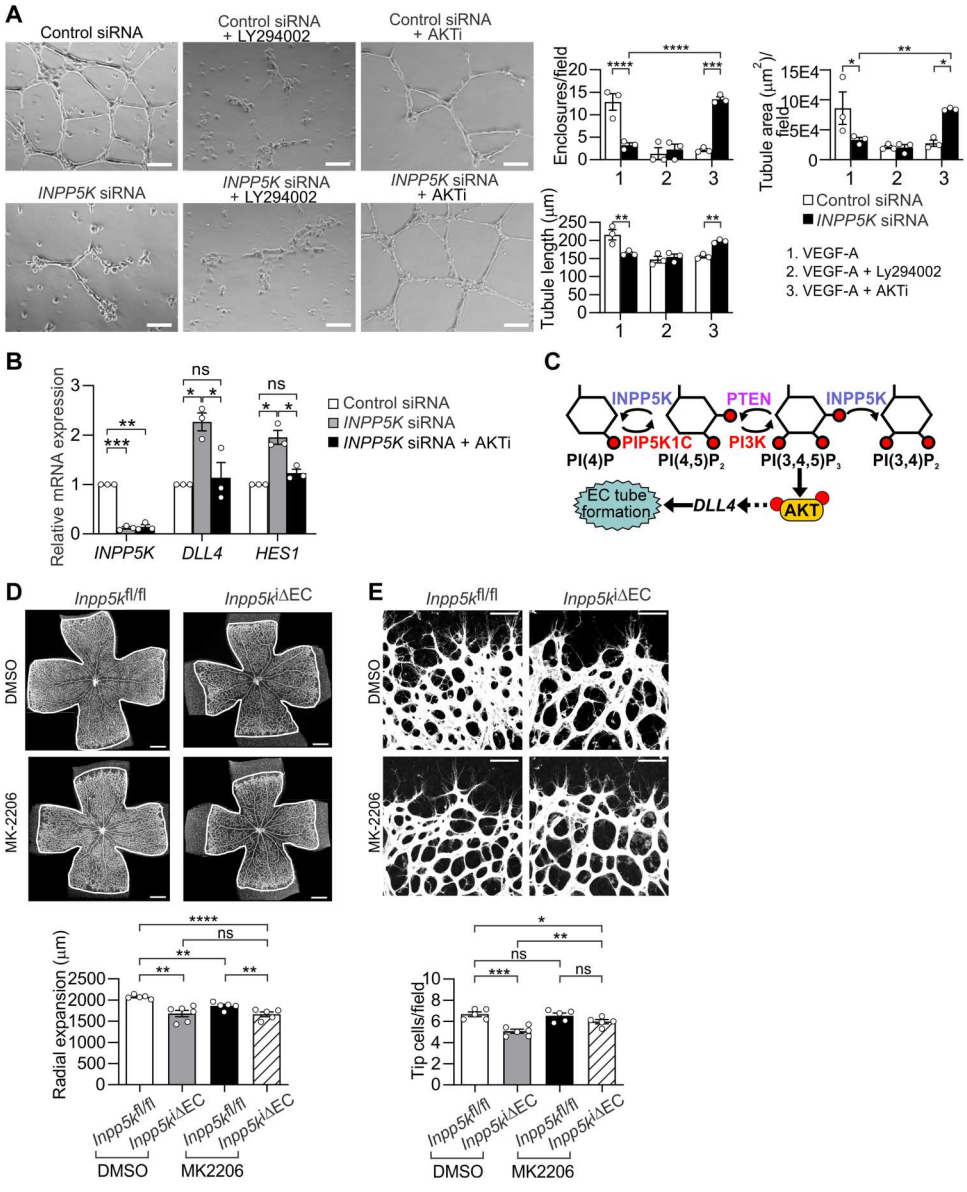

Fig. 8. AKT inhibition rescues enhanced NOTCH pathway activation and restores tip cells. (**A**) Bright-field images of *INPP5K*-siRNA HUVEC tube formation on Matrigel for 16 hours in medium with VEGF-A (50 ng/ml) ± 2.5 μM LY294002 or ± 5 μM pan AKT inhibitor. Scale bars, 125 μm. Graphs: Interconnected tubule enclosures, tubule length, and area, as means ± SEM of three independent experiments. Statistics by ANOVA followed by Tukey's post hoc test. **P* < 0.05, ***P* < 0.01, ****P* < 0.001, and *****P* < 0.0001. AKT inhibition rescues *INPP5K*-siRNA HUVECs tube defects. (**B**) NOTCH pathway effectors analyzed by qRT-PCR of mRNA from *INPP5K*-siRNA HUVECs grown on Matrigel for 16 hours with VEGF-A (50 ng/ml) ± 5 μM pan AKT inhibitor. GAPDH is endogenous control. Graph: Mean relative mRNA expression ± SEM of three independent experiments. Statistics by ANOVA followed by Tukey's post hoc test. **P* < 0.05, ***P* < 0.01, and ****P* < 0.001. Enhanced NOTCH pathway activation in *INPP5K*-siRNA HUVECs rescued with AKT inhibition. (**C**) INPP5K limits $PI(4,5)P_2$ availability for PI3K-mediated $PI(3,4,5)P_3$ generation and AKT activation influencing NOTCH pathway activation and EC tube formation. (**D**) Confocal images of endomucin-stained flat-mount *Inpp5k*$^{fl/fl}$ and *Inpp5k*$^{i\Delta EC}$ P7 retina from mice treated with 100 μg of MK2206 or DMSO vehicle, showing radial vascular expansion. Scale bars, 500 μm. Graph: Radial vascular expansion ± SEM of five retinas per genotype. Statistics by ANOVA, followed by Tukey's post hoc test. ***P* < 0.01 and *****P* < 0.0001. AKT inhibition does not restore vascular expansion in *Inpp5k*$^{i\Delta EC}$ retina. (**E**) Confocal images of endomucin-stained flat-mount *Inpp5k*$^{fl/fl}$ and *Inpp5k*$^{i\Delta EC}$ P7 retina from mice treated with 100 μg of MK2206 or DMSO-vehicle. Scale bars, 50 μm. Graph: Tip cell number ± SEM. Statistics by ANOVA, followed by Tukey's post hoc test. **P* < 0.05, ***P* < 0.01, and ****P* < 0.001. AKT inhibition rescues impaired tip cell numbers in *Inpp5k*$^{i\Delta EC}$ retinal vasculature. See also fig. S8.

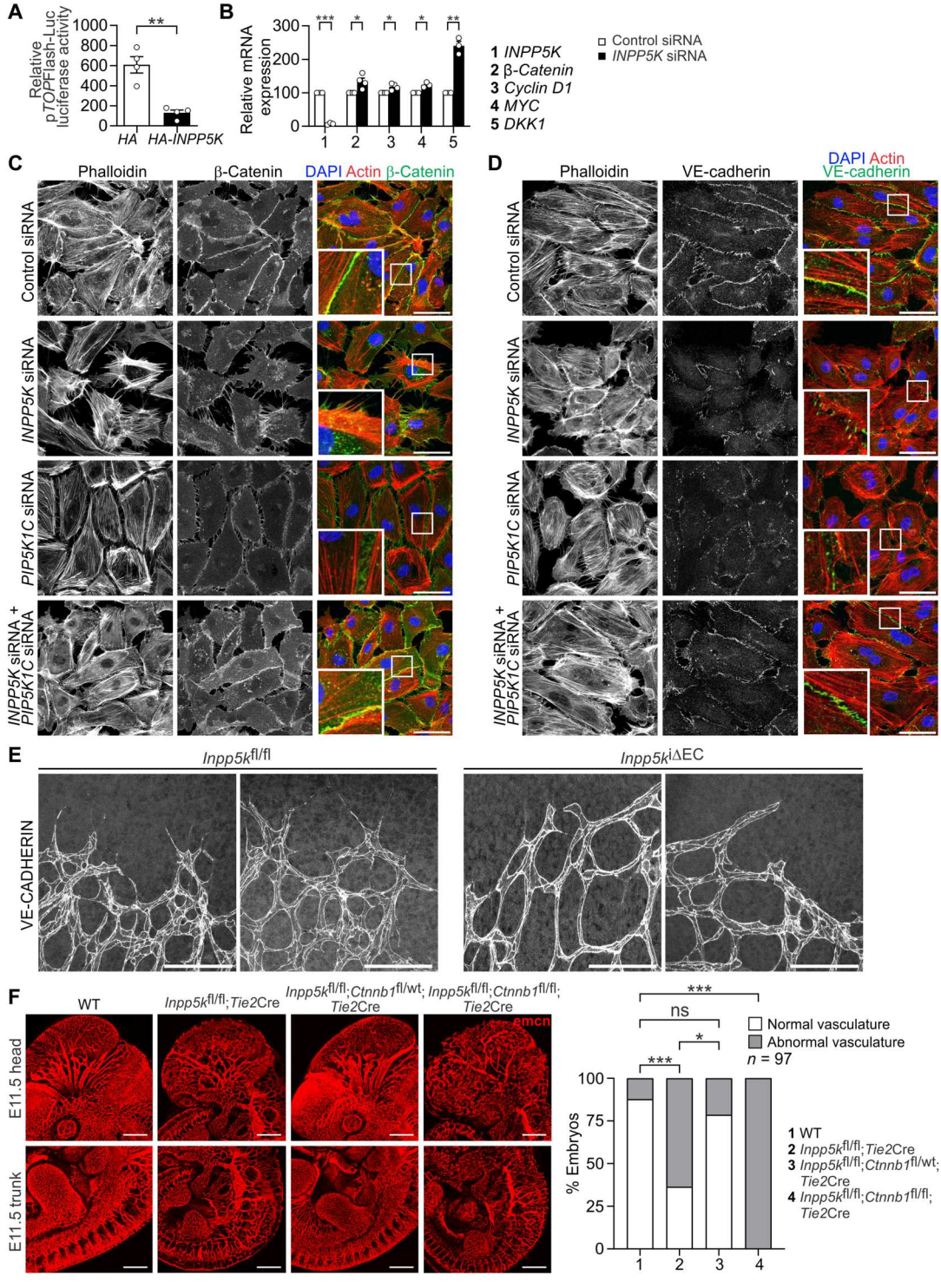

Fig. 9. INPP5K regulates β-catenin transcriptional activity. (**A**) COS1 cells transfected with p*TOP*Flash firefly luciferase reporter plasmid, thymidine kinase *Renilla* luciferase control plasmid, and indicated HA-*INPP5K* or HA-vector plasmids. Relative activity is the ratio of *TOP*Flash firefly luciferase/*Renilla* luciferase ± SEM of four independent experiments. Comparison of means by Student's *t* test for unpaired data. $^{**}P < 0.01$. *INPP5K* suppresses p*TOP*Flash-Luc transcriptional activation. (**B**) mRNA from confluent *INPP5K*-siRNA HUVECs or controls analyzed by qRT-PCR with GAPDH as endogenous control. Graph: mRNA transcription ± SEM, four independent experiments. Comparison of means by Student's *t* test for unpaired data. $^{*}P < 0.05$, $^{**}P < 0.01$, and $^{***}P < 0.001$. *INPP5K* depletion increases β-catenin–TCF/LEF transcriptional activation. (**C**) Confocal images of HUVECs stained with β-catenin antibodies, DAPI, and phalloidin. Images of confluent cell monolayers at similar confluency. Scale bars, 50 μm. White boxes shown at increased magnification in lower left quadrants for β-catenin at cell membrane. *INPP5K* depletion reduces β-catenin membrane localization, restored with knockdown of *PIP5K1C*. (**D**) Confocal images of HUVECs stained with antibodies to VE-cadherin and counterstained with DAPI and phalloidin. Images representative of confluent cell monolayers with similar cell confluency. Scale bars, 50 μm. White boxes shown at increased magnification in lower left quadrants display VE-cadherin at membrane. *INPP5K* depletion decreases VE-cadherin membrane association, restored with *PIP5K1C* knockdown. (**E**) Confocal images of flat-mount P6 $Inpp5k^{fl/fl}$ or $Inpp5k^{i\Delta EC}$ retina stained with antibodies to VE-cadherin. Scale bars, 100 μm. INPP5K deletion alters cell morphology at vascular front. (**F**) Confocal images of endomucin-stained whole-mount E11.5 WT, $Inpp5k^{fl/fl}$;*Tie2*Cre, $Inpp5k^{fl/fl}$;$Ctnnb1^{fl/wt}$;*Tie2*Cre, or $Inpp5k^{fl/fl}$;$Ctnnb1^{fl/fl}$;*Tie2*Cre embryos, showing the vascular plexus of the head (top) or trunk (bottom). Scale bars, 500 μm. Graph: Percent embryos with normal or abnormal vasculature ($n = 97$ embryos). Independent groups compared by two-tailed Fisher's exact test. $^{*}P < 0.05$ and $^{***}P < 0.001$. Heterozygous β-catenin deletion, in part, rescues $Inpp5k^{fl/fl}$;*Tie2*Cre embryo abnormal vasculature. See also fig. S9.

plasmids into CV1 SV40 (COS1) cells with concomitant ectopic expression of *HA-INPP5K* to examine the effect of increased INPP5K expression on β-catenin transcriptional activation. Ectopic expression of *HA-INPP5K* in COS1 cells suppressed transcriptional activation of p*TOP*Flash-Luc (Fig. 9A). Conversely, transcription of β-catenin (*CTNNB1*) and its responsive TCF/LEF target genes *CYCLIN D1*, *MYC*, and *DKK1* were increased in *INPP5K*-siRNA HUVECs (Fig. 9B). Thus, altered expression of INPP5K influences TCF/LEF transcriptional activation.

A major pathway for induction of β-catenin–mediated transcriptional activation is through Wnt ligand binding to the Frizzled receptor and its co-receptors Low-density lipoprotein receptor-related protein (LRP5/6) (*71*). Wnt ligand engagement with FZD/LRP5/6 decreases GSK3β-mediated phosphorylation of β-catenin at $Thr^{41}/Ser^{33}/Ser^{37}$, leading to stabilization and accumulation of β-catenin (*72*). AKT can also stabilize β-catenin independent of Wnt through inhibition of GSK3β, preventing β-catenin phosphorylation at $Ser^{33/37}/Thr^{41}$ within the β-catenin destruction complex and thereby suppressing its proteasomal degradation (*73*). Therefore, we examined the phosphorylation status and stability of β-catenin by immunoblot analysis using antibodies against total β-catenin and non–phospho-($Thr^{41}/Ser^{33}/Ser^{37}$)–β-catenin. *INPP5K*-siRNA HUVECs showed a decrease in total β-catenin, independent of VEGF stimulation, with a similar decrease in dephosphorylated β-catenin (fig. S9A). While we cannot exclude the contribution of Wnt signaling to our phenotype, these data are inconsistent with Wnt activation through FZD/LRP5/6 and argue against a prominent role for Wnt ligand activation of β-catenin in the context of INPP5K loss. Equally, although we observe increased phosphorylation of AKT and GSK3β (Fig. 7A), this did not alter β-catenin phosphorylation or result in increased β-catenin stabilization (fig. S9A). We interpret these data to indicate that in the context of INPP5K loss, PI3K/AKT signaling does not affect phosphorylation of GSK3β within the β-catenin destruction complex to regulate β-catenin stability and transcriptional activation and is consistent with studies that show that β-catenin transcriptional activity is not directly regulated by PI3K/AKT-mediated effects on the β-catenin destruction complex (*74*). In addition, Wnt-mediated inhibition of GSK3 and β-catenin stabilization is reported to be independent of AKT-mediated phosphorylation of GSK3β at Ser^{9} (*75*, *76*). We therefore examined the involvement of alternative mechanisms of β-catenin activation in the context of INPP5K loss of function.

Endothelial-dependent angiogenesis requires the closely coordinated interactions of adherens junctions, which are contingent on the dynamics of VE-cadherin (*Cdh5*), linked through its cytoplasmic domain to p120-catenin, β-catenin, or plakoglobin (*64*). Murine inactivation of *Cdh5* or truncation of the β-catenin binding domain of *Cdh5* is embryonic lethal because of impaired angiogenesis, vascular regression, and endocardial defects (*77*, *78*), and inducible deletion of *Cdh5* in the murine retina enhances angiogenic sprouting (*79*). Decreased junctional stability leads to release of β-catenin from adherens junctions, which promotes β-catenin nuclear translocation and increases transcriptional activation independent of Wnt ligand (*64*). Evolving evidence suggests a level of interconnectivity between VEGFR2/NOTCH pathway activation and junctional remodeling in the endothelium (*80*–*82*), which prompted us to question whether INPP5K affected β-catenin transcriptional activity by regulating the subcellular localization of β-catenin.

Epithelial cell-cell junctions formed by apical adherens junctions are composed of cadherin adhesion molecules that interact dynamically with the cortical actin cytoskeleton (*83*). To examine junctional remodeling, we first examined cell morphology by phalloidin staining of filamentous actin in *INPP5K*-siRNA HUVECs (Fig. 9, C and D, and fig. S9B). Filamentous actin bundling appeared increased and disrupted in *INPP5K*-siRNA HUVECs, and cells showed EC retraction and disruption of cell-cell contacts; the latter was highlighted by VE-cadherin staining. These morphological changes in *INPP5K*-siRNA HUVECs were corrected following concomitant transfection of *PIP5K1C*-siRNA, which reduces $PI(4,5)P_2$ but not with p110α or AKT inhibition (Fig. 9, C and D, and fig. S9B). The complex morphology of *INPP5K*-siRNA HUVECs increased the difficulty of interpreting junctional localization of β-catenin, and therefore, any assessment of β-catenin localization at the cell periphery was limited to the plasma membrane, identified by phalloidin staining of submembranous actin. Examination of endothelial junctions by staining with the tight junction marker zonula occludens–1 (ZO-1) showed evidence of disordered endothelial junctions in *INPP5K*-siRNA HUVECs (fig. S9B). Continuous β-catenin staining at the cell periphery was demonstrated in control cells, together with a highly concentrated localization in the perinuclear region (Fig. 9C). *INPP5K* depletion in HUVECs reduced β-catenin localization at the cell periphery, concomitant with an expanded perinuclear distribution (Fig. 9C), indicating that with INPP5K reduction, β-catenin is released from the cell membrane and recruited to the perinuclear endocytic recycling compartment, a subcellular site where β-catenin localizes before its nuclear entry, increasing its availability for nuclear import (*84*). To determine the contribution of phosphoinositide regulation by INPP5K, β-catenin localization was reexamined in HUVECs with concomitant depletion of *INPP5K* and *PIP5K1C* or in *INPP5K*-siRNA HUVECs treated with p110α or AKT inhibitors. *PIP5K1C* depletion alone reduced β-catenin localization at the cell periphery but retained its highly concentrated perinuclear localization (Fig. 9C). Notably, β-catenin membrane localization was restored with concomitant knockdown of both *PIP5K1C* and *INPP5K* (Fig. 9C) but not in *INPP5K*-siRNA cells treated with the p110α inhibitor BYL719 or the AKT inhibitor MK2206 (fig. S9C), indicating a requirement for $PI(4,5)P_2$ but not PI3K/AKT regulation by INPP5K in maintaining β-catenin membrane localization.

PIP5K1C directly associates with the classical cadherin complexes E-cadherin, N-cadherin, and VE-cadherin, and $PI(4,5)P_2$ generated by PIP5K1C at cadherin contact sites enhances adherens junction assembly and maturation (*85*). Control siRNA HUVECs showed robust membranous VE-cadherin localization (Fig. 9D); however, recruitment of VE-cadherin to the cell membrane in *INPP5K*-siRNA HUVECs was markedly reduced, with discontinuous VE-cadherin staining (Fig. 9D), associated with reduced VE-cadherin protein as assessed by immunoblot analysis (fig. S9D), which is consistent with increased VE-cadherin internalization, which has been reported to be stimulated for other cadherins by increased $PI(4,5)P_2$ and subsequent proteasome-mediated degradation (*85*, *86*). Here, association of VE-cadherin to the cell membrane was also disrupted in *PIP5K1C*-siRNA HUVECs (Fig. 9D). Notably, robust VE-cadherin staining at the membrane and VE-cadherin degradation was restored with concurrent

silencing of both the PI(4,5)P_2 5-phosphatase *INPP5K* and the PI(4)P 5-kinase *PIP5K1C* (Fig. 9D and fig. S9E) but not with inhibition of p110α or AKT (fig. S9, F and G). Collectively, these data are indicative of a PI(4,5)P_2-dependent defect in VE-cadherin membrane association in *INPP5K*-siRNA ECs, which results in reduced β-catenin at the cell membrane. We speculate that this is a consequence of increased PI(4,5)P_2, which stimulates increased VE-cadherin internalization as has been reported for E-cadherin (*85*).

VE-cadherin localization was also examined in vivo at the advancing vascular front of P6 *Inpp5k*$^{i\Delta EC}$ murine retina. A serrated VE-cadherin staining pattern was observed at the EC membrane at the advancing retinal vascular front of control mice as previously reported (*3*, *80*, *87*). However, ECs at the vascular front in *Inpp5k*$^{i\Delta EC}$ retina exhibited continuous VE-cadherin staining (Fig. 9E). Because the morphology of ECs at the vascular front of control retina was complex with multiple tip cells and filopodial protrusions while, in *Inpp5k*$^{i\Delta EC}$ retina, this complex pattern of staining was lost, associated with loss of tip cells (Fig. 9E), we cannot exclude the possibility that these changes in morphology alter the apparent distribution of VE-cadherin.

As endothelial-specific gain-of-function β-catenin mutants exhibit a vascular phenotype reminiscent of *Inpp5k*$^{-/-}$ embryos, with embryonic lethality midgestation due to impaired angiogenesis accompanied by increased *Dll4* transcription (*60*), we further validated a role for β-catenin in the *Inpp5k*-null vascular phenotype by crossing *Inpp5k*$^{fl/fl}$;*Tie2*Cre mice with *Ctnnb1*$^{fl/fl}$ lines to generate concurrent endothelial-specific deletion of INPP5K and β-catenin. Embryos were examined at E11.5, 1 day after expected *Inpp5k*$^{fl/fl}$;*Tie2*Cre embryonic death. Sixty-four percent *Inpp5k*$^{fl/fl}$;*Tie2*Cre embryos were growth retarded and displayed impaired angiogenesis (Fig. 9F). Heterozygous deletion of *Ctnnb1* combined with homozygous deletion of *Inpp5k* resulted in normal vasculature and embryonic growth of 78% *Inpp5k*$^{fl/fl}$;*Ctnnb1*$^{fl/wt}$;*Tie2*Cre embryos, with only 22% growth retarded (Fig. 9F). However, homozygous deletion of both *Inpp5k* and *Ctnnb1* caused extensive vascular defects and severe growth retardation in 100% *Inpp5k*$^{fl/fl}$;*Ctnnb1*$^{fl/fl}$;*Tie2*Cre embryos (Fig. 9F). These findings demonstrate a dose-dependent genetic interaction between INPP5K and β-catenin during embryonic angiogenesis.

Collectively, these data are consistent with a model in which regulation of PI(4,5)P_2 by INPP5K affects β-catenin–dependent *NOTCH* effector transcription. INPP5K cooperates with PIP5K1C to maintain PI(4,5)P_2-dependent VE-cadherin/β-catenin membrane localization, which constrains β-catenin availability for nuclear import. In parallel, INPP5K limits PI(4,5)P_2 substrate availability to regulate PI(3,4,5)P_3-dependent AKT activation. We propose that any influence of AKT on β-catenin transcriptional activation to promote NOTCH effector transcription can only occur in the context of high PI(4,5)P_2, which facilitates β-catenin release from the cell membrane, thereby allowing hyperactive AKT to contribute to enhanced *DLL4* transcription. Thus, INPP5K turnover of PI(4,5)P_2 in the endothelial membrane acts as a gateway licensing β-catenin–mediated transcription of NOTCH effectors that affect tip cell specification.

DISCUSSION

Here, we demonstrate that the PI(4,5)P_2 5-phosphatase, INPP5K, plays an EC-autonomous role that is essential for effective embryonic and postnatal angiogenesis. We propose a model whereby INPP5K regulation of PI(4,5)P_2 facilitates cross-talk between VE-cadherin/β-catenin and AKT in ECs to license a β-catenin/DLL4/NOTCH signaling nexus necessary for tip cell specification (Fig. 10).

Regulation of PI3K/AKT signaling has emerged as a critical component for effective angiogenesis (*5*, *7*, *8*). We show here that loss of INPP5K increased PI(3,4,5)P_3 and thereby AKT and FOXO1 phosphorylation; however, our phenotype is not consistent with murine models of altered PI3K signaling as a consequence of either inactivation of p110α, FOXO1, or PTEN (*5*, *7*, *54*, *88*). PI3K/AKT signaling increases NOTCH pathway activation in ECs (*61*, *67*), and conversely, ectopic expression of activated NOTCH increases AKT phosphorylation (*89*), suggesting a reciprocal regulatory relationship between PI3K/AKT and NOTCH signaling. However, in vivo studies suggest a considerable level of complexity within PI3K/AKT signaling and NOTCH pathway activation that remains to be defined. *DLL4* transcription is only repressed following combined pharmacological inhibition of both p110α and p110δ in syngeneic tumor models (*88*) but not during developmental angiogenesis, where EC-specific inactivation of p110α has no effect on endothelial tip cell specification (*5*). Endothelial depletion of *Akt1* does not alter tip/stalk cell identity or DLL4 expression in retinal vasculature (*8*). PTEN, which inactivates PI3K/AKT signaling, plays no regulatory role in NOTCH pathway activation or endothelial tip cell specification but restricts vessel density selectively at the vascular front through suppression of EC proliferation via both phosphatase-dependent and nuclear phosphatase–independent mechanisms (*7*). Thus, regulation of PI3K-generated PI(3,4,5)P_3/AKT signaling alone does not appear to be sufficient to regulate NOTCH pathway activation or direct tip cell specification during developmental angiogenesis. It is notable that although INPP5K and PTEN both degrade PI(3,4,5)P_3 signals and thereby both suppress AKT signaling, INPP5K has an additional key substrate, PI(4,5)P_2, which is not hydrolyzed by PTEN. We show here in multiple experimental models that reduced expression or ablation of INPP5K significantly increased PI(4,5)P_2 and thereby contributed to β-catenin localization. We propose that AKT contributes to β-catenin–mediated transcription of NOTCH effectors but only in the context of high PI(4,5)P_2 signaling, which facilitates β-catenin release from VE-cadherin at the cell membrane. The lack of functional redundancy between PTEN and INPP5K suggests that hydrolysis of PI(4,5)P_2 by INPP5K and degradation of PI(3,4,5)P_3 by PTEN are both essential for effective angiogenesis, facilitating tip and stalk cell specification, respectively.

We show that endothelial regulation of PI(4,5)P_2 by INPP5K contributes to β-catenin–dependent *NOTCH* effector transcription. Here, PI(4,5)P_2 accumulation as a consequence of INPP5K ablation, decreased VE-cadherin association with the membrane, associated with β-catenin membrane dissociation and NOTCH effector transcription. VE-cadherin membrane localization was not regulated by PI(3,4,5)P_3 or activation of AKT, as its reduced plasma membrane localization in *INPP5K*-siRNA cells was not rescued by PI3K or AKT inhibition. However, AKT hyperactivation does contribute to INPP5K-null angiogenesis defects, as AKT inhibition fully

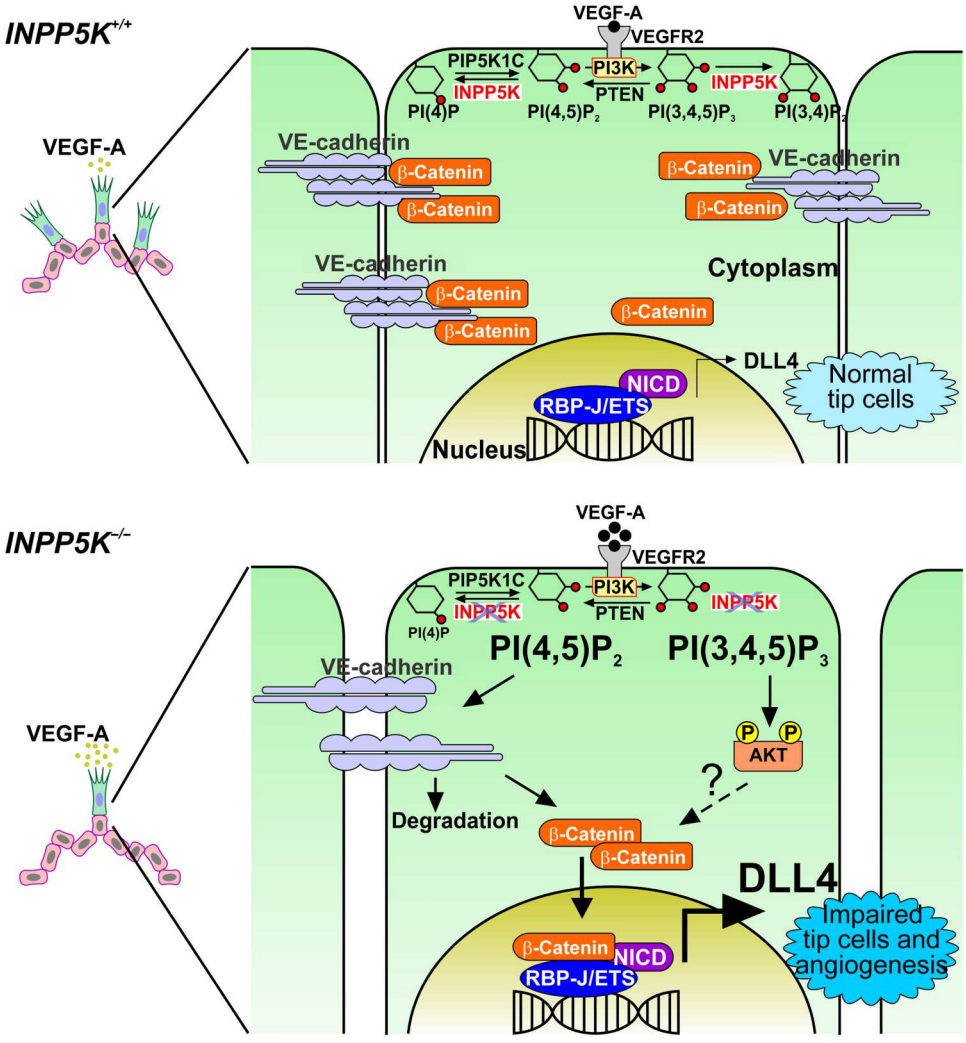

Fig. 10. Endothelial cell signaling regulated by INPP5K. Model depicting INPP5K regulation of $PI(4,5)P_2$ licenses a β-catenin/DLL4/NOTCH signaling nexus to facilitate endothelial tip cell selection.

restored tube formation defects, attenuated NOTCH effector transcription in *INPP5K*-siRNA ECs, and rescued tip cell defects in *Inpp5k*$^{i\Delta EC}$ murine retinal vasculature. Therefore, our interpretation of these data is that AKT contributes to β-catenin–mediated transcription of NOTCH effectors but only under conditions of high $PI(4,5)P_2$, which facilitates VE-cadherin/β-catenin release from the plasma membrane with INPP5K ablation. Our model is consistent with studies showing that PI3K/AKT signaling can induce formation of β-catenin/NICD transcriptional complexes that enhance DLL4/NOTCH pathway activation (*66*–*68*). In addition, INPP5K-null angiogenesis defects are reminiscent of endothelial-specific gain-of-function β-catenin mutants, which exhibit embryonic lethal defective angiogenesis, associated with increased *DLL4* transcription and up-regulation of endothelial NOTCH signaling (*60*). In support of this argument, deletion of a single allele of *Ctnnb1* in the endothelium restored angiogenesis in EC-specific INPP5K-null embryos, indicating a dose-dependent genetic interaction between *Inpp5k* and *Ctnnb1*.

Our evidence suggests that INPP5K hydrolysis of $PI(4,5)P_2$ in ECs plays a principal role in the regulation of tip cell specification. $PI(4,5)P_2$ metabolism is central to numerous biological processes, and emerging studies indicate that $PI(4,5)P_2$ may play a role in vascular development. For example, phospholipase C (PLC), which hydrolyzes $PI(4,5)P_2$ to generate inositol trisphosphate and diacylglycerol, contributes to vasculogenesis, hematopoiesis, arterial differentiation, and vascular regression, but not angiogenesis (*13*). ORP2 (oxysterol-binding protein-related protein 2; *Osbpl2*), a cholesterol-$PI(4,5)P_2$ exchange transporter, suppresses endothelial tip cell density via regulation of VEGFR2 proteolytic cleavage and VE-cadherin expression (*12*); however, the role of ORP2 in developmental angiogenesis remains to be defined, as *Osbpl2* knockout mice and zebrafish are viable and exhibit normal vascular development (*12*, *90*). Similarly, paladin, a $PI(4,5)P_2$ phosphatase, suppresses endothelial retinal tip cell sprouting through VEGFR2 internalization and ERK1/2 signaling (*14*), yet despite expression of paladin in embryonic vasculature, *Pald1*-null mice are viable and show normal embryonic angiogenesis (*91*). Cytidine

diphosphate diacylglycerol (CDP-DAG) synthase 2 catalyzes CDP-DAG formation, the rate limiting step in de novo phosphatidylinositol biosynthesis, thereby controlling phosphoinositide recycling. Angiogenesis is impaired in *Cds2* zebrafish mutants and morphants, and neovascularization is impeded in xenograft tumor models (*15*, *16*). Tip cell density is reduced in *Cds2*-null retinal vessels; however, inhibition of NOTCH did not restore angiogenesis defects of *Cds2* zebrafish mutants (*16*). Instead, ablation of *Cds2* prevented VEGF-A–induced phosphoinositide recycling, reducing $PI(4,5)P_2$ availability, to limit $PI(3,4,5)P_3$ generation, thus permitting FOXO1-mediated vascular regression (*16*).

Here, we provide compelling evidence from murine and cell culture models supporting a role for INPP5K regulation of $PI(4,5)P_2$ signaling in NOTCH pathway activation. Ablation of INPP5K in embryos or ECs increased expression of the NOTCH ligand *DLL4*, the NOTCH receptor *NOTCH4*, and the downstream transcriptional effector *HES1*. Endothelial-specific *Dll4*, *Notch1*, and *Notch4* gain-of-function models show vascular defects highly reminiscent of $Inpp5k^{-/-}$ embryos (*92*–*94*). However, *Dll4* and *Notch1* gain-of-function mutants also display arteriovenous malformations (*92*, *93*), which are not a feature of $Inpp5k^{-/-}$ embryos, while arteriovenous specification is normal in *Notch4* gain-of-function embryos (*94*). Here, *Inpp5k* ablation enhanced *Dll4* and *Notch4* transcripts, but *Notch1* transcription was unaffected. Whether the $Inpp5k^{-/-}$ vascular phenotype is the result of specific activation of NOTCH4 signaling in response to DLL4 ligation remains a subject of future investigation. In proof-of-principle experiments, inhibition of NOTCH or DLL4 restored impaired EC tube formation in *INPP5K*-siRNA ECs. Crucially, NOTCH inhibition rescued defective angiogenesis and extended embryonic viability of $Inpp5k^{-/-}$ embryos and restored tip cell specification in $Inpp5k^{i\Delta EC}$ neonatal retinal vessels. These data provide powerful evidence that NOTCH pathway activation contributes to impaired tip cell specification and angiogenesis in *Inpp5k* knockout embryos and neonates.

Recessive mutations in *INPP5K* have been identified in consanguineous families that cause congenital muscular dystrophy, cognitive impairment, and early-onset cataracts, associated with decreased $PI(4,5)P_2$ 5-phosphatase activity (*19*, *20*). Impaired angiogenesis was not described; however, the homozygous missense and compound heterozygous *INPP5K* mutations associated with disease only partially impair INPP5K $PI(4,5)P_2$ 5-phosphatase activity, suggesting that they represent hypomorphic alleles. We propose that *INPP5K* is an essential gene and that complete loss is incompatible with life. Here, $Inpp5k^{-/-}$ mice die from angiogenic defects from E10.5, a period before the successive waves of myogenic differentiation that occur during embryonic limb bud myogenesis from E10.5 to E16 (*95*). Evidence is also emerging that impaired angiogenesis may contribute to muscle diseases (*96*); therefore, it will be of interest to examine an association between angiogenesis and the muscular dystrophy phenotype in these affected individuals. We present our model as an original viewpoint that identifies an unappreciated role for $PI(4,5)P_2$ in the endothelium, which contributes to a β-catenin/NOTCH/DLL4 signaling nexus to define tip cell specification, critical for both embryonic and postnatal angiogenesis.

MATERIALS AND METHODS

Reagents

HUVECs and EGM-2 medium were obtained from Lonza. COS1 cells were purchased from the American Type Culture Collection. VEGF-A and bFGF were from Sigma-Aldrich and Thermo Fisher Scientific, respectively. Rat anti-endomucin antibody (14-5851-85) was from eBioscience. Cy3-conjugated anti-SMA (A2547) antibody and fluorescein isothiocyanate–conjugated isolectin B4 (IB4; L2895) were from Sigma-Aldrich. Antibodies to human INPP5K have been previously described (*97*). Antibodies to AKT (4685), $pSer^{473}$-AKT (4058), $pThr^{308}$-AKT (2965), $pSer^{33/37}/Thr^{41}$–β-catenin (9561), $pSer^{235/236}$-S6 (4858), $pSer^{256}$-FOXO1 (9461), FOXO1 (2880), $pSer^{9}$-GSK3b (9323), GSK3b (9315), $pThr^{202}/Tyr^{204}$-ERK1/2 (9106), ERK1/2 (4695), VE-cadherin (2500), cleaved caspase-3 (9664), and $pSer^{10}$–histone H3 (3377) were from Cell Signaling Technology. ZO-1 (40-2200), ZO-1 (ZO1-1A12), β-tubulin (322600), glyceraldehyde-3-phosphate dehydrogenase (GAPDH; am4300), glutathione *S*-transferase (GST; 71-7500), Alexa Fluor 488–conjugated phalloidin (A12379), Ki67 (RM-9106-S0), 4′,6-diamidino-2-phenylindole (DAPI), and Alexa Fluor–conjugated secondary antibodies were from Thermo Fisher Scientific. $PI(3,4,5)P_3$ (Z-P345B), $PI(3,4)P_2$ (Z-P034), $PI(4,5)P_2$ (Z-PO45), and PI(4)P (Z-P004) antibodies were from Echelon Biosciences. Goat anti-DLL4 antibody (AF1389) was from R&D Systems. Collagen IV (21501470) was from Bio-Rad. Pan-actin (MS-1295-P) was from Neomarkers. Tamoxifen was from Sigma-Aldrich. GFR-Matrigel (354230) and antibodies to CD31 (550274), mouse CD144 (555289), human CD144 (555661), and β-catenin (610153) were from BD Biosciences. DLL4-Fc (ALX-201-386) was obtained from Enzo Life Sciences. NG2 (AB5320) antibodies and AKT inhibitor X (CAS 925681-41-0) were from Merck Millipore. γ-Secretase inhibitor DAPT was purchased from Sigma-Aldrich. Pimonidazole hydrochloride plus antibody (HP1-200kit) was obtained from Hypoxyprobe Inc. PI3K inhibitor LY294002 was from Sigma-Aldrich. PI3Kα inhibitor BYL719 and AKT inhibitor MK2206 were obtained from Selleckchem. RNA isolation kit and gene-specific qRT-PCR primers were obtained from QIAGEN. *Inpp5k*-specific qRT-PCR and other genotyping primers were synthesized at Geneworks. Oligofectamine and LTX Plus transfection reagents were purchased from Thermo Fisher Scientific. GFP-PH/Btk construct was provided by T. Balla [National Institutes of Health (NIH)]. YFP-PH-TAPP1 construct was provided by D. Alessi (University of Dundee). GST-Fab1p, YOTB, Vac1p, EEA1 (FYVE)/Hepatocyte growth factor-regulated tyrosine kinase substrate (Hrs) construct was provided by T. Takenawa (Kobe University).

Generation of *Inpp5k* knockout mice

Exon 8 of *Inpp5k* was flanked with *LoxP* sites by homologous recombination in C57BL/6-derived murine embryonic stem cells (Ozgene Pty Ltd., Australia). Recombination at the correct locus was confirmed by Southern hybridization of Bam HI–digested embryonic stem cells with 5′ and 3′ probes. Cre-mediated deletion of exon 8 results in frameshift and truncation of INPP5K at amino acid 277, resulting in a polypeptide that lacks several critical residues (D287, R288, D329, H330, P332, and V333), essential for 5-phosphatase enzyme activity. Neomycin cassette of the targeted allele was removed by mating with the Flippase recombinase (FLPe)

transgenic line to obtain the *Inpp5k*$^{fl/+}$ line, confirmed with Southern hybridization and PCR genotyping of genomic DNA isolated from tail biopsies. *Inpp5k*$^{fl/+}$ mice were bred with mice expressing Cre under control of the *CMV* promoter to obtain *Inpp5k* heterozygotes, which were intercrossed to generate global *Inpp5k* knockout mice. *Inpp5k*$^{fl/fl}$ mice were bred with mice expressing Cre under control of the endothelial *Tie2* promoter to generate endothelial-specific *Inpp5k* knockout mice (*Inpp5k*$^{fl/fl}$;*Tie2Cre*). *Inpp5k*$^{fl/fl}$;*Tie2Cre* mice were intercrossed with *Ctnnb1*$^{fl/fl}$ (*98*) mice to generate mice with concurrent endothelial-specific deletion of INPP5K and β-catenin. *Inpp5k*$^{fl/fl}$ mice were crossed with mice expressing tamoxifen-activated Cre under the control of the endothelial *Cdh5* promoter [*Cdh5*(PAC)-CreERT2] to generate tamoxifen-inducible EC-specific *Inpp5k* knockout mice (*Inpp5k*$^{i\Delta EC}$). All mice were on a C57BL/6 background. Pups were generated by natural mating, and embryos were generated by timed mating. For timed mating, the morning of vaginal plug observation was assigned E0.5. No specific gender was selected for analysis. Mice were housed at Monash Animal Research Platform laboratories on a 12-hour light/12-hour dark cycle with food and water provided ad libitum. Mice were euthanized by CO_2 asphyxiation and cervical dislocation. All animal work was carried out following the National Health and Medical Research Council Australia Code for Care and Use of Animals for Scientific Purposes (eighth edition, 2013) and was approved by the Monash University Animal Ethics Committee.

Genotyping

Targeted embryonic stem cells were genotyped by Southern hybridization. Mice and embryos were genotyped by PCR of genomic DNA isolated from tail biopsies or yolk sacs. PCR of *Inpp5k* wild-type and knockout alleles was carried out with forward primer 5′-cagcttcattcataaactcctgggc and reverse primer 5′-cagtaggtaataagcatgatggaactc with 35 cycles of 94°C for 30 s, 62°C for 30 s, and 72°C for 30 s. The *Tie2-Cre* transgene was identified with primers 5′-cgcataaccagtgaaacagcattgc and 5′-ccctgtgctcagacagaaatgaga, with 35 PCR cycles of 94°C for 30 s, 66°C for 60 s, and 72°C for 30s, and included internal control primers 5′-ctaggccacagaattgaaagatct and 5′-gtaggtggaaattctagcatcatcc. PCR of *Inpp5k* floxed alleles was performed with forward primer 5′-caagtctgagtctctacaacttcag and reverse primer 5′-caacctccacaggatgcggtcag with 5 cycles of 94°C for 30 s, 65°C for 60 s, and 72°C for 30 s, followed by 30 cycles of 94°C for 30 s, 62°C for 60 s, and 72°C for 30 s. PCR of *Ctnnb1* floxed alleles was performed with forward primer 5′-actgcctttgttctcttcccttctg and reverse primer 5′-cagccaaggagagcaggtgagg with 30 cycles of 94°C for 30 s, 70°C for 30 s, and 72°C for 30 s.

Whole-mount embryo immunofluorescence

Isolated embryos were fixed in 4% paraformaldehyde for 30 min, washed in phosphate-buffered saline (PBS), and dehydrated through increasing methanol concentrations [25, 50, 75, and 100% methanol (+PBS) series]. Embryos were then incubated in Dent's buffer [methanol:dimethyl sulfoxide (DMSO):hydrogen peroxide; 4:1:1] for 2 hours, followed by rehydration in decreasing methanol concentrations [100, 75, 50, and 25% (+PBS) series]. Following transfer to PBS, embryos were incubated in blocking buffer [100 mM maleic acid, 1% DMSO, and 10% horse serum in PBS (pH 7.6)] for 1 hour and then incubated overnight at 4°C with primary antibodies diluted in blocking buffer. After extensive washing with PBTX (PBS with 0.05% Triton X-100), embryos were incubated with fluorescent-tagged secondary antibodies in PBTX overnight at 4°C. Multiple *z*-plane stacked images were obtained by confocal laser scanning microscopy (Nikon C1) with 4× Plan Fluor NA 0.13, 10× Plan Fluor NA 0.30, 20× Plan Fluor NA 0.75 multi-immersion, or 40× Plan Fluor NA 1.30 oil immersion objective lenses. Embryonic hindbrain and dorsal longitudinal anastomotic vessel vasculatures were stained as described above and were mounted onto microscopy slides.

Matrigel plug assay

Six-week-old *Inpp5k*$^{fl/fl}$ or *Inpp5k*$^{fl/fl}$;*Cdh5*(PAC)-CreERT2 mice were administered 500 μg of tamoxifen dissolved in corn oil and ethanol (9:1) daily for five consecutive days to generate control and endothelial-specific *Inpp5k* knockout (*Inpp5k*$^{i\Delta EC}$) mice, respectively. Mice were subcutaneously injected with 500 μl of growth factor–reduced Matrigel supplemented with 500 ng of bFGF or 250 ng of VEGF. Matrigel containing PBS was used as a negative control. Plugs were removed after 2 weeks, fixed in formalin, and paraffin-embedded. Sections (5 μm) were deparaffinized and subjected to antigen retrieval in citrate buffer [10 mM sodium citrate (pH 6.0)]. Sections were incubated in blocking medium [5% (v/v) goat serum in PBS] for 1 hour followed by incubation with endomucin antibodies in blocking medium overnight. After PBS wash, the sections were incubated with Alexa Fluor 555–conjugated secondary antibodies and counterstained with DAPI. Sections were imaged at multiple random positions with a confocal laser scanning microscope (Nikon C1) using 40× Plan Fluor NA 1.30 oil immersion objective. The proportion of endomucin-positive area was calculated in de-identified samples using ImageJ software (NIH).

Tumor angiogenesis

Six-week-old *Inpp5k*$^{fl/fl}$ or *Inpp5k*$^{fl/fl}$;*Cdh5*(PAC)-CreERT2 mice were administered 500 μg of tamoxifen dissolved in corn oil and ethanol (9:1) daily for five consecutive days to generate control and endothelial-specific *Inpp5k* knockout (*Inpp5k*$^{i\Delta EC}$) mice, respectively. Mice were injected subcutaneously with 2×10^6 LLC or B16F10 melanoma cells in 100 μl of PBS into the right abdominal flank. Once palpable, tumors were measured using digital calipers, and tumor volumes were calculated using the formula: (length × width × width)/2. Tumors were fixed overnight in formalin and processed for paraffin-embedding. Thin tumor sections (5 μm) were deparaffinized and subjected to antigen-retrieval in citrate buffer [10 mM sodium citrate (pH 6.0)], EDTA buffer [1 mM EDTA (pH 8.0)], or commercial epitope retrieval buffer (Leica, 6074383). Sections were incubated in blocking medium [5% (v/v) goat serum in PBS] for 1 hour followed by incubation with endomucin, Ki67, Cy3-SMA, collagen IV, or cleaved caspase-3 primary antibodies in blocking medium overnight. After PBS wash, the sections were incubated with Alexa Fluor 488– or Alexa Fluor 555–conjugated secondary antibodies and counterstained with DAPI. Each tumor section was imaged at multiple random positions with a confocal laser scanning microscope (Nikon C1) using 40× Plan Fluor NA 1.30 oil immersion objective. Calculations were performed on de-identified samples using ImageJ software (NIH).

Hypoxia assay

Tumor-bearing mice were administered pimonidazole hydrochloride (60 mg/kg) intraperitoneally 90 min before euthanasia. Paraffin tumor sections were prepared and subjected to antigen retrieval as described above. Tumor areas with hypoxia were detected with anti-pimonidazole antibody and visualized with Alexa Fluor 488–conjugated secondary antibodies. Each tumor section was imaged at multiple random positions with a confocal laser scanning microscope (Nikon C1) using 40× Plan Fluor NA 1.30 oil immersion objective. The proportion of hypoxic area in de-identified samples was calculated using ImageJ software (NIH).

Postnatal retinal angiogenesis

Inpp5k$^{fl/fl}$;*Cdh5*(PAC)-CreERT2 pups were intragastrically administered 50 μg of tamoxifen dissolved in corn oil and ethanol (9:1) on P1, P2, and P3, and retinas were collected on P5, P6, or P7. Retinas were isolated and fixed in 2% paraformaldehyde or ice-cold methanol for 2 hours. Retinas were permeabilized and blocked with 1% bovine serum albumin (BSA) and 0.3% Triton X-100 in PBS. Retinas were washed with Pblec buffer [1 mM $CaCl_2$, 1 mM $MgCl_2$, 0.1 mM $MnCl_2$, and 1% Triton X-100 in PBS (pH 6.8)] and incubated overnight at 4°C in primary antibodies diluted in Pblec. Following PBTX wash, retinas were incubated overnight at 4°C with appropriate Alexa Fluor–conjugated secondary antibodies diluted in Pblec and flat-mounted onto microscopy slides. Multiple *z*-plane stacked retinal images were obtained by confocal laser scanning microscopy (Nikon C1) with 4× Plan Fluor NA 0.13, 10× Plan Fluor NA 0.30, 20× Plan Fluor NA 0.75 multi-immersion, or 40× Plan Fluor NA 1.30 oil immersion objective lenses, and de-identified samples were analyzed using ImageJ software (NIH).

Quantitative RT-PCR

mRNA was isolated from E9.5 embryo lysates, neonatal lungs, or HUVECs. For examination of NOTCH pathway effectors in HUVECs, mRNA was isolated from cells that were plated on GFR Matrigel for 16 hours. mRNA was reverse-transcribed, and cDNA was amplified using commercially available specific primers, with GAPDH as an endogenous control. *Inpp5k*-specific primers were designed in-house (forward, 5′-ccagctgctccgcgagttcc and reverse, 5′-acggctgccgcttcaacctc). Cycling was performed with SYBR Green on a Rotor-Gene 3000 (Corbett Research), and differential expression was determined using comparative $\Delta\Delta C_t$.

Cell culture and transient siRNA transfection

HUVECs were maintained in EGM-2 medium (Lonza). Early-passage (P4) HUVECs were transiently transfected with siRNA oligonucleotides or scrambled control oligonucleotides using Oligofectamine transfection reagent according to the manufacturer's instructions (INPP5K siRNA#1 sense sequence, 5′-GCCAAGU GUCGUCCACAUATT-3′; INPP5K siRNA#2 sense sequence, 5′-GGAAUUAGCCGCUUAAAUATT-3′; PIP5K1A siRNA#1 sense sequence, 5′-GCCUCUUGAUGUCAAUCCATT-3′; PIP5K1A siRNA#2 sense sequence, 5′-CUGCCUUGAUAAUAUGUU ATT-3′; PIP5K1C siRNA#1 sense sequence, 5′-GCGUCGGU GGUCAUGAACAATT-3′; and PIP5K1C siRNA#2 sense sequence, 5′-CGCCCGCCACCGACAUUATT-3′). Experiments were performed 48 hours after transfection.

Transwell migration assays

HUVECs were dissociated with Versene solution (Thermo Fisher Scientific). Cells (0.5×10^5) resuspended in 100 μl of low-serum (0.5%) medium were seeded into the upper chamber of a 6.5-mm-diameter, 8-μm pore Transwell plate (Corning Inc.) and allowed to migrate toward the lower chamber of the Transwell plate containing 600 μl of complete growth media and VEGF-A (50 ng/ml) ± 5 μM DAPT or 5 μg/ml DLL4-Fc for 5 hours. Non-migrating cells on the upper surface of the Transwell membrane were removed with a cotton swab, and migrating cells on the lower surface of the Transwell membrane were fixed, stained (Diff-Quik kit; Lab Aids P/L), and visualized using light microscopy (Olympus IX71) with a 10× Cplan FL NA 0.3 RC1 dry objective lens. The number of migrating cells across 12 fields per condition was quantified in de-identified samples using ImageJ software (NIH).

In vitro endothelial tube formation assay

Twelve-well plates were coated with GFR Matrigel (300 μl) before incubation at 37°C for 30 min. HUVECs were dissociated with Versene solution, and 7.5×10^4 cells were plated onto the polymerized Matrigel and overlaid with endothelial growth medium containing VEGF-A (50 ng/ml). Sixteen hours after seeding, representative bright-field images (>12 per condition) were collected (AF6000LX; Leica) using a 10× NA 0.30 PH1 dry objective lens. Quantification of branch point number, tubule number, average tubule length, tubule area, and the number of interconnected tubule enclosures was assessed in de-identified samples with ImageJ software. For inhibitor studies, the overlaid medium contained 2.5 μM LY294002, 5 μM DAPT, DLL4-Fc (5 μg/ml), or 5 μM AKT inhibitor or vehicle controls. To determine live-to-dead cell ratios during tube formation, cells were stained with Hoechst 33342 (Sigma-Aldrich), a live cell marker, and propidium iodide (Sigma-Aldrich), a dead cell marker.

Cell viability assay

Cell viability was assessed using CellTiter-Glo 3D Cell Viability Assay (Promega, catalog no. G9681). Matrigel (75 μl) was aliquoted intro a 48-well plate and incubated at 37°C for 30 min. HUVECs were suspended using 1 mM EDTA in PBS. HUVECs (2.0×10^4) were seeded onto Matrigel and overlaid with 100 μl of EGM-2 endothelial growth media plus VEGF-A (50 ng/ml) and incubated at 37°C for 16 hours. The medium was removed and replaced with 100 μl of endothelial growth medium plus 100 μl of CellTiter reagent at room temperature. The plate was shaken for 5 min to induce cell lysis and incubated for 30 min to stabilize the luminescent signal. The integrated luminescent signal was detected using a BMG Labtech CLARIOstar Plus plate reader with CLARIOstar version 5.20 R5 and MARS 3.10 R6 software.

Inhibitor treatment of embryos and retina

Plug-mated dams were administered DAPT (50 μg/g body weight) at E7.5, E8.5, and E9.5 via tail vein injection. Embryos were collected at E10.5 or E11.5, and vasculature was visualized by whole-mount immunostaining with anti-endomucin as described above. E11.5 embryos were also examined for the presence of heartbeats during dissection. *Inpp5k*$^{i\Delta EC}$ pups were injected subcutaneously with DAPT (200 μg) or MK2206 (100 μg) or DMSO at P4 and P5. Retinas were collected at P7, and vasculature was visualized by

immunostaining with anti-endomucin and flat-mounted as described above. Multiple *z*-plane stacked images were obtained by confocal laser scanning microscopy (Nikon C1) with 4× Plan Fluor NA 0.13, 10× Plan Fluor NA 0.30, 20× Plan Fluor NA 0.75 multi-immersion, or 40× Plan Fluor NA 1.30 oil immersion objective lenses, and de-identified samples were analyzed using ImageJ software (NIH).

Immunoblot analysis

HUVECs were serum-starved for 5 hours before stimulation with VEGF-A (100 ng/ml). Nonidet P-40 (NP-40)–soluble cell fractions or whole-cell lysates were resolved by SDS–polyacrylamide gel electrophoresis. For inhibitor studies, cells were exposed to 1 μM BYL719 or 1 μM MK2206 for 24 hours. Relative protein was assessed by densitometry (ImageQuant TL software; GE Healthcare) of nonsaturated exposures of immunoblot films and standardized against appropriate loading controls.

Indirect immunofluorescence

HUVECs grown in a confluent monolayer on glass coverslips were fixed with 4% electron microscopy (EM) grade paraformaldehyde for 10 min at 37°C, permeabilized for 15 min in PBS containing 0.1% Triton X-100, and then blocked in PBS containing 2% BSA. Cells were counterstained with DAPI and Alexa Fluor–conjugated phalloidin. Cells were incubated with primary antibodies in PBS containing 0.1% BSA for 3 hours at room temperature. Single *z*-plane images or *z*-plane stacked images were obtained by confocal laser scanning microscopy (TCS-NT SP5, Leica) with 40× HCX Plan-Apochromat NA 1.25 λBL or 100× HCX Plan-Apochromat NA 1.4 CS oil immersion objective lenses. Plasma membrane phosphoinositide accumulation was assessed as previously described (*44*). Single *z*-plane images were obtained by confocal laser scanning microscopy (TCS-NT SP5, Leica) with 40× HCX Plan-Apochromat NA 1.25 λBL or 100× HCX Plan-Apochromat NA 1.4 CS oil immersion objective lenses. Quantification of phosphoinositide accumulation was performed in de-identified samples using ImageJ software, determined by measuring the average pixel fluorescence intensity within an area of defined size drawn over three distinct areas of the plasma membrane (5 × 10 pixels) or the average of three boxes (10 × 10 pixels) in the cytosol, and expressed as ratios of plasma membrane to cytosolic pixel fluorescence intensity (*29*).

Biosensor recruitment to the plasma membrane

HUVECs grown in a confluent monolayer on glass coverslips were transfected with GFP-PH/Btk (*48*) or YFP-PH/TAPP1 (*47*) using Lipofectamine LTX Plus according to the manufacturer′s protocol. Twenty-four hours after transfection, cells were serum-starved for 5 hours, treated with VEGF-A (100 ng/ml), and fixed with 4% paraformaldehyde for 20 min. Single *z*-plane images were obtained by confocal laser scanning microscopy (TCS-NT SP5, Leica) with 40× HCX Plan-Apochromat NA 1.25 λBL or 100× HCX Plan-Apochromat NA 1.4 CS oil immersion objective lenses, and de-identified samples were analyzed using ImageJ software. Quantification of plasma membrane biosensor recruitment was determined by measuring the average pixel fluorescence intensity within an area of defined size drawn over three distinct areas of the plasma membrane (5 × 10 pixels) or the average of three boxes (10 × 10 pixels) in the cytosol and expressed as ratios of plasma membrane to cytosolic pixel fluorescence intensity (*29*).

GST-FYVE overlay assay

The method was adapted from the work of Hammond *et al.* (*44*). HUVECs grown in a confluent monolayer were fixed in 2% paraformaldehyde for 15 min and washed in PBS containing 50 mM NH_4Cl. Cells were washed in buffer A [20 mM Pipes, 137 mM NaCl, and 2.7 mM KCL (pH 6.8)], permeabilized with digitonin, and then blocked in blocking buffer (buffer A, 5% goat serum, and 50 mM NH_4Cl). Cells were incubated with GST-FYVE Hrs recombinant protein (2 μg/ml in buffer A containing 5% goat serum) for 1 hour at room temperature, washed with buffer A, and then incubated with GST antibodies for 1 hour at room temperature. After washing, cells were incubated with appropriate secondary antibodies for 45 min at room temperature, postfixed in 2% paraformaldehyde, and washed with PBS containing 50 mM NH_4Cl. Single *z*-plane images were obtained by confocal laser scanning microscopy (TCS-NT SP5, Leica) with 40× HCX Plan-Apochromat NA 1.25 λBL oil immersion objective lens.

Droplet digital PCR

mRNA (50 ng) was reverse-transcribed into cDNA using iScript gDNA Clear cDNA Synthesis Kit (Bio-Rad) according to the manufacturer′s protocol. Droplet digital PCR was performed using the Bio-Rad QX200 Droplet Digital PCR system (Bio-Rad Laboratories, Hercules, CA). Reactions (20 μl) containing 1× ddPCR EvaGreen Supermix (Bio-Rad), 1× primers, and cDNA (8.3 ng/μl) were loaded into the middle wells of a droplet generator cartridge, and 70 μl of Droplet Generation Oil for EvaGreen was loaded into the lower wells. Thermal cycling was performed on generated droplets, with detection identified with a QX200 droplet reader. Data were analyzed using QuantaSoft software (Bio-Rad) with detection thresholds set manually according to no template controls.

Luciferase reporter assay

The p*TOP*Flash-Luc reporter gene vector (reporter plasmid containing multiple copies of wild-type TCF binding sites upstream of the Thymidine Kinase minimal promoter and Luciferase open reading frame) and p*FOP*Flash-Luc vector control (reporter plasmid containing mutant TCF-binding sites) were provided by H. Clevers (Hubrecht Institute, Utrecht, The Netherlands). COS1 cells were maintained in Dulbecco′s modified Eagle′s medium (DMEM) supplemented with 10% (v/v) fetal bovine calf serum, 2 mM L-glutamine, penicillin (100 U/ml), and 0.1% (v/v) streptomycin. COS1 cells were cotransfected with p*TOP*Flash-Luc or p*FOP*-Flash-Luc vector control and phRL-Tk (*Renilla*) and either hemagglutinin (HA)–tagged full-length human *INPP5K* or vector alone using Lipofectamine LTX Plus according to the manufacturer′s protocol. Cells were lysed 24 hours after transfection, and luciferase activities of cell lysates were determined using the Dual-Luciferase Reporter (DLR) Assay System (Promega). Transfection efficiency of each sample was normalized to *Renilla* activity.

Statistical analysis

Statistical significance of comparison between the means of two groups was assessed using the two-tailed Student′s *t* test for unpaired data. Significance of multiple comparisons of sample means was performed with one-way analysis of variance

(ANOVA) followed by Tukey's post hoc test. (GraphPad Prism version 8.4.2). Comparison of independent groups was examined using two-tailed Fisher's exact test. *P* values less than 0.05 were considered statistically significant.

Supplementary Materials

This PDF file includes:

Figs. S1 to S9

View/request a protocol for this paper from *Bio-protocol*.

REFERENCES AND NOTES

1. P. Carmeliet, Angiogenesis in health and disease. *Nat. Med.* **9**, 653–660 (2003).
2. H. Gerhardt, VEGF and endothelial guidance in angiogenic sprouting. *Organogenesis* **4**, 241–246 (2008).
3. L. Jakobsson, C. A. Franco, K. Bentley, R. T. Collins, B. Ponsioen, I. M. Aspalter, I. Rosewell, M. Busse, G. Thurston, A. Medvinsky, S. Schulte-Merker, H. Gerhardt, Endothelial cells dynamically compete for the tip cell position during angiogenic sprouting. *Nat. Cell Biol.* **12**, 943–953 (2010).
4. M. Graupera, M. Potente, Regulation of angiogenesis by PI3K signaling networks. *Exp. Cell Res.* **319**, 1348–1355 (2013).
5. M. Graupera, J. Guillermet-Guibert, L. C. Foukas, L.-K. Phng, R. J. Cain, A. Salpekar, W. Pearce, S. Meek, J. Millan, P. R. Cutillas, A. J. H. Smith, A. J. Ridley, C. Ruhrberg, H. Gerhardt, B. Vanhaesebroeck, Angiogenesis selectively requires the p110α isoform of PI3K to control endothelial cell migration. *Nature* **453**, 662–666 (2008).
6. K. Hamada, T. Sasaki, P. A. Koni, M. Natsui, H. Kishimoto, J. Sasaki, N. Yajima, Y. Horie, G. Hasegawa, M. Naito, J.-i. Miyazaki, T. Suda, H. Itoh, K. Nakao, T. W. Mak, T. Nakano, A. Suzuki, The PTEN/PI3K pathway governs normal vascular development and tumor angiogenesis. *Genes Dev.* **19**, 2054–2065 (2005).
7. H. Serra, I. Chivite, A. Angulo-Urarte, A. Soler, J. D. Sutherland, A. Arruabarrena-Aristorena, A. Ragab, R. Lim, M. Malumbres, M. Fruttiger, M. Potente, M. Serrano, À. Fabra, F. Viñals, O. Casanovas, P. P. Pandolfi, A. Bigas, A. Carracedo, H. Gerhardt, M. Graupera, PTEN mediates Notch-dependent stalk cell arrest in angiogenesis. *Nat. Commun.* **6**, 7935 (2015).
8. M. Y. Lee, A. K. Luciano, E. Ackah, J. Rodriguez-Vita, T. A. Bancroft, A. Eichmann, M. Simons, T. R. Kyriakides, M. Morales-Ruiz, W. C. Sessa, Endothelial Akt1 mediates angiogenesis by phosphorylating multiple angiogenic substrates. *Proc. Natl. Acad. Sci. U.S.A.* **111**, 12865–12870 (2014).
9. T. Balla, Phosphoinositides: Tiny lipids with giant impact on cell regulation. *Physiol. Rev.* **93**, 1019–1137 (2013).
10. S. Choi, N. Thapa, X. Tan, A. C. Hedman, R. A. Anderson, PIP kinases define PI4,5P2 signaling specificity by association with effectors. *Biochim. Biophys. Acta* **1851**, 711–723 (2015).
11. J. M. Dyson, C. G. Fedele, E. M. Davies, J. Becanovic, C. A. Mitchell, Phosphoinositide phosphatases: Just as important as the kinases. *Subcell. Biochem.* **58**, 215–279 (2012).
12. A. Koponen, G. Pan, A. M. Kivelä, A. Ralko, J. H. Taskinen, A. Arora, R. Kosonen, O. K. Kari, J. Ndika, E. Ikonen, W. Cho, D. Yan, V. M. Olkkonen, ORP2, a cholesterol transporter, regulates angiogenic signaling in endothelial cells. *FASEB J.* **34**, 14671–14694 (2020).
13. H. J. Liao, T. Kume, C. McKay, M.-J. Xu, J. N. Ihle, G. Carpenter, Absence of erythrogenesis and vasculogenesis in Plcg1-deficient mice. *J. Biol. Chem.* **277**, 9335–9341 (2002).
14. A. Nitzsche, R. Pietilä, D. T. Love, C. Testini, T. Ninchoji, R. O. Smith, E. Ekvärn, J. Larsson, F. P. Roche, I. Egaña, S. Jauhiainen, P. Berger, L. Claesson-Welsh, M. Hellström, Paladin is a phosphoinositide phosphatase regulating endosomal VEGFR2 signalling and angiogenesis. *EMBO Rep.* **22**, e50218 (2021).
15. A. N. Stratman, O. M. Farrelly, C. M. Mikelis, M. F. Miller, Z. Wang, V. N. Pham, A. E. Davis, M. C. Burns, S. A. Pezoa, D. Castranova, J. J. Yano, T. M. Kilts, G. E. Davis, J. S. Gutkind, B. M. Weinstein, Anti-angiogenic effects of VEGF stimulation on endothelium deficient in phosphoinositide recycling. *Nat. Commun.* **11**, 1204 (2020).
16. W. Zhao, L. Cao, H. Ying, W. Zhang, D. Li, X. Zhu, W. Xue, S. Wu, M. Cao, C. Fu, H. Qi, Y. Hao, Y.-C. Tang, J. Qin, T. P. Zhong, X. Lin, L. Yu, X. Li, L. Li, D. Wu, W. Pan, Endothelial CDS2 deficiency causes VEGFA-mediated vascular regression and tumor inhibition. *Cell Res.* **29**, 895–910 (2019).
17. M. Jacoby, J. J. Cox, S. Gayral, D. J. Hampshire, M. Ayub, M. Blockmans, E. Pernot, M. V. Kisseleva, P. Compère, S. N. Schiffmann, F. Gergely, J. H. Riley, D. Pérez-Morga, C. G. Woods, S. Schurmans, INPP5E mutations cause primary cilium signaling defects, ciliary instability and ciliopathies in human and mouse. *Nat. Genet.* **41**, 1027–1031 (2009).
18. T. Kawano, Y. Indo, H. Nakazato, M. Shimadzu, I. Matsuda, Oculocerebrorenal syndrome of Lowe: Three mutations in the OCRL1 gene derived from three patients with different phenotypes. *Am. J. Med. Genet.* **77**, 348–355 (1998).
19. D. P. S. Osborn, H. L. Pond, N. Mazaheri, J. Dejardin, C. J. Munn, K. Mushref, E. S. Cauley, I. Moroni, M. B. Pasanisi, E. A. Sellars, R. S. Hill, J. N. Partlow, R. K. Willaert, J. Bharj, R. A. Malamiri, H. Galehdari, G. Shariati, R. Maroofian, M. Mora, L. E. Swan, T. Voit, F. J. Conti, Y. Jamshidi, M. C. Manzini, Mutations in INPP5K cause a form of congenital muscular dystrophy overlapping Marinesco-Sjögren syndrome and dystroglycanopathy. *Am. J. Hum. Genet.* **100**, 537–545 (2017).
20. M. Wiessner, A. Roos, C. J. Munn, R. Viswanathan, T. Whyte, D. Cox, B. Schoser, C. Sewry, H. Roper, R. Phadke, C. Marini Bettolo, R. Barresi, R. Charlton, C. G. Bönnemann, O. Abath Neto, U. C. Reed, E. Zanoteli, C. Araújo Martins Moreno, B. Ertl-Wagner, R. Stucka, C. de Goede, T. Borges da Silva, D. Hathazi, M. Dell'Aica, R. P. Zahedi, S. Thiele, J. Müller, H. Kingston, S. Müller, E. Curtis, M. C. Walter, T. M. Strom, V. Straub, K. Bushby, F. Muntoni, L. E. Swan, H. Lochmüller, J. Senderek, Mutations in INPP5K, encoding a phosphoinositide 5-phosphatase, cause congenital muscular dystrophy with cataracts and mild cognitive impairment. *Am. J. Hum. Genet.* **100**, 523–536 (2017).
21. S. L. Bielas, J. L. Silhavy, F. Brancati, M. V. Kisseleva, L. al-Gazali, L. Sztriha, R. A. Bayoumi, M. S. Zaki, A. Abdel-Aleem, R. O. Rosti, H. Kayserili, D. Swistun, L. C. Scott, E. Bertini, E. Boltshauser, E. Fazzi, L. Travaglini, S. J. Field, S. Gayral, M. Jacoby, S. Schurmans, B. Dallapiccola, P. W. Majerus, E. M. Valente, J. G. Gleeson, Mutations in INPP5E, encoding inositol polyphosphate-5-phosphatase E, link phosphatidyl inositol signaling to the ciliopathies. *Nat. Genet.* **41**, 1032–1036 (2009).
22. T. Ijuin, Y. Mochizuki, K. Fukami, M. Funaki, T. Asano, T. Takenawa, Identification and characterization of a novel inositol polyphosphate 5-phosphatase. *J. Biol. Chem.* **275**, 10870–10875 (2000).
23. A. C. Schmid, H. M. Wise, C. A. Mitchell, R. Nussbaum, R. Woscholski, Type II phosphoinositide 5-phosphatases have unique sensitivities towards fatty acid composition and head group phosphorylation. *FEBS Lett.* **576**, 9–13 (2004).
24. T. Ijuin, T. Takenawa, SKIP negatively regulates insulin-induced GLUT4 translocation and membrane ruffle formation. *Mol. Cell. Biol.* **23**, 1209–1220 (2003).
25. T. Ijuin, Y. E. Yu, K. Mizutani, A. Pao, S. Tateya, Y. Tamori, A. Bradley, T. Takenawa, Increased insulin action in SKIP heterozygous knockout mice. *Mol. Cell. Biol.* **28**, 5184–5195 (2008).
26. M. J. McGrath, M. J. Eramo, R. Gurung, A. Sriratana, S. M. Gehrig, G. S. Lynch, S. R. Lourdes, F. Koentgen, S. J. Feeney, M. Lazarou, C. A. McLean, C. A. Mitchell, Defective lysosome reformation during autophagy causes skeletal muscle disease. *J. Clin. Invest.* **131**, e135124 (2021).
27. Y. Y. Kisanuki, R. E. Hammer, J. I. Miyazaki, S. C. Williams, J. A. Richardson, M. Yanagisawa, Tie2-Cre transgenic mice: A new model for endothelial cell-lineage analysis in vivo. *Dev. Biol.* **230**, 230–242 (2001).
28. Y. Wang, M. Nakayama, M. E. Pitulescu, T. S. Schmidt, M. L. Bochenek, A. Sakakibara, S. Adams, A. Davy, U. Deutsch, U. Lüthi, A. Barberis, L. E. Benjamin, T. Mäkinen, C. D. Nobes, R. H. Adams, Ephrin-B2 controls VEGF-induced angiogenesis and lymphangiogenesis. *Nature* **465**, 483–486 (2010).
29. E. M. Davies, A. M. Kong, A. Tan, R. Gurung, A. Sriratana, P. E. Bukczynska, L. M. Ooms, C. A. McLean, T. Tiganis, C. A. Mitchell, Differential SKIP expression in PTEN-deficient glioblastoma regulates cellular proliferation and migration. *Oncogene* **34**, 3711–3727 (2015).
30. T. Zygmunt, S. Trzaska, L. Edelstein, J. Walls, S. Rajamani, N. Gale, L. Daroles, C. Ramírez, F. Ulrich, J. Torres-Vázquez, 'In parallel' interconnectivity of the dorsal longitudinal anastomotic vessels requires both VEGF signaling and circulatory flow. *J. Cell Sci.* **125**, 5159–5167 (2012).
31. F. Milde, S. Lauw, P. Koumoutsakos, M. L. Iruela-Arispe, The mouse retina in 3D: Quantification of vascular growth and remodeling. *Integr. Biol.* **5**, 1426–1438 (2013).
32. M. Poulet, J. Sirois, K. Boyé, N. Uetani, S. Hardy, T. Daubon, A. Dubrac, M. L. Tremblay, A. Bikfalvi, PRL-2 phosphatase is required for vascular morphogenesis and angiogenic signaling. *Commun. Biol.* **3**, 603 (2020).
33. H. Park, H. Yamamoto, L. Mohn, L. Ambühl, K. Kanai, I. Schmidt, K.-P. Kim, A. Fraccaroli, S. Feil, H. J. Junge, E. Montanez, W. Berger, R. H. Adams, Integrin-linked kinase controls retinal angiogenesis and is linked to Wnt signaling and exudative vitreoretinopathy. *Nat. Commun.* **10**, 5243 (2019).
34. M. Corada, F. Orsenigo, M. F. Morini, M. E. Pitulescu, G. Bhat, D. Nyqvist, F. Breviario, V. Conti, A. Briot, M. L. Iruela-Arispe, R. H. Adams, E. Dejana, Sox17 is indispensable for acquisition and maintenance of arterial identity. *Nat. Commun.* **4**, 2609 (2013).
35. C. Raimondi, A. Fantin, A. Lampropoulou, L. Denti, A. Chikh, C. Ruhrberg, Imatinib inhibits VEGF-independent angiogenesis by targeting neuropilin 1-dependent ABL1 activation in endothelial cells. *J. Exp. Med.* **211**, 1167–1183 (2014).
36. J. Zink, M. Frye, T. Frömel, C. Carlantoni, D. John, D. Schreier, A. Weigert, H. Laban, G. Salinas, H. Stingl, L. Günther, R. Popp, J. Hu, B. Vanhollebeke, H. Schmidt, A. Acker-Palmer, T. Renné,

I. Fleming, P. M. Benz, EVL regulates VEGF receptor-2 internalization and signaling in developmental angiogenesis. *EMBO Rep.* **22**, e48961 (2021).
37. A. Benn, F. Alonso, J. Mangelschots, E. Génot, M. Lox, A. Zwijsen, BMP-SMAD1/5 signaling regulates retinal vascular development. *Biomolecules* **10**, 488 (2020).
38. R. Benedito, C. Roca, I. Sörensen, S. Adams, A. Gossler, M. Fruttiger, R. H. Adams, The Notch ligands Dll4 and Jagged1 have opposing effects on angiogenesis. *Cell* **137**, 1124–1135 (2009).
39. I. Arnaoutova, H. K. Kleinman, In vitro angiogenesis: Endothelial cell tube formation on gelled basement membrane extract. *Nat. Protoc.* **5**, 628–635 (2010).
40. G. Carpentier, S. Berndt, S. Ferratge, W. Rasband, M. Cuendet, G. Uzan, P. Albanese, Angiogenesis analyzer for ImageJ—A comparative morphometric analysis of "endothelial tube formation assay" and "fibrin bead assay". *Sci. Rep.* **10**, 11568 (2020).
41. A. M. Goodwin, In vitro assays of angiogenesis for assessment of angiogenic and anti-angiogenic agents. *Microvasc. Res.* **74**, 172–183 (2007).
42. P. Nowak-Sliwinska, K. Alitalo, E. Allen, A. Anisimov, A. C. Aplin, R. Auerbach, H. G. Augustin, D. O. Bates, J. R. van Beijnum, R. H. F. Bender, G. Bergers, A. Bikfalvi, J. Bischoff, B. C. Böck, P. C. Brooks, F. Bussolino, B. Cakir, P. Carmeliet, D. Castranova, A. M. Cimpean, O. Cleaver, G. Coukos, G. E. Davis, M. de Palma, A. Dimberg, R. P. M. Dings, V. Djonov, A. C. Dudley, N. P. Dufton, S. M. Fendt, N. Ferrara, M. Fruttiger, D. Fukumura, B. Ghesquière, Y. Gong, R. J. Griffin, A. L. Harris, C. C. W. Hughes, N. W. Hultgren, M. L. Iruela-Arispe, M. Irving, R. K. Jain, R. Kalluri, J. Kalucka, R. S. Kerbel, J. Kitajewski, I. Klaassen, H. K. Kleinmann, P. Koolwijk, E. Kuczynski, B. R. Kwak, K. Marien, J. M. Melero-Martin, L. L. Munn, R. F. Nicosia, A. Noel, J. Nurro, A. K. Olsson, T. V. Petrova, K. Pietras, R. Pili, J. W. Pollard, M. J. Post, P. H. A. Quax, G. A. Rabinovich, M. Raica, A. M. Randi, D. Ribatti, C. Ruegg, R. O. Schlingemann, S. Schulte-Merker, L. E. H. Smith, J. W. Song, S. A. Stacker, J. Stalin, A. N. Stratman, M. van de Velde, V. W. M. van Hinsbergh, P. B. Vermeulen, J. Waltenberger, B. M. Weinstein, H. Xin, B. Yetkin-Arik, S. Yla-Herttuala, M. C. Yoder, A. W. Griffioen, Consensus guidelines for the use and interpretation of angiogenesis assays. *Angiogenesis* **21**, 425–532 (2018).
43. G. R. V. Hammond, S. K. Dove, A. Nicol, J. A. Pinxteren, D. Zicha, G. Schiavo, Elimination of plasma membrane phosphatidylinositol (4,5)-bisphosphate is required for exocytosis from mast cells. *J. Cell Sci.* **119**, 2084–2094 (2006).
44. G. R. V. Hammond, G. Schiavo, R. F. Irvine, Immunocytochemical techniques reveal multiple, distinct cellular pools of PtdIns$_4$P and PtdIns(4,5)P$_2$. *Biochem. J.* **422**, 23–35 (2009).
45. M. Malek, A. Kielkowska, T. Chessa, K. E. Anderson, D. Barneda, P. Pir, H. Nakanishi, S. Eguchi, A. Koizumi, J. Sasaki, V. Juvin, V. Y. Kiselev, I. Niewczas, A. Gray, A. Valayer, D. Spensberger, M. Imbert, S. Felisbino, T. Habuchi, S. Beinke, S. Cosulich, N. L. Novère, T. Sasaki, J. Clark, P. T. Hawkins, L. R. Stephens, PTEN regulates PI(3,4)P$_2$ signaling downstream of class I PI3K. *Mol. Cell* **68**, 566–580.e10 (2017).
46. S. C. Yip, R. J. Eddy, A. M. Branch, H. Pang, H. Wu, Y. Yan, B. E. Drees, P. O. Neilsen, J. Condeelis, J. M. Backer, Quantification of PtdIns(3,4,5)P3 dynamics in EGF-stimulated carcinoma cells: A comparison of PH-domain-mediated methods with immunological methods. *Biochem. J.* **411**, 441–448 (2008).
47. W. A. Kimber, L. Trinkle-Mulcahy, P. C. F. Cheung, M. Deak, L. J. Marsden, A. Kieloch, S. Watt, R. T. Javier, A. Gray, C. P. Downes, J. M. Lucocq, D. R. Alessi, Evidence that the tandem-pleckstrin-homology-domain-containing protein TAPP1 interacts with Ptd(3,4)P2 and the multi-PDZ-domain-containing protein MUPP1 in vivo. *Biochem. J.* **361**, 525–536 (2002).
48. P. Várnai, T. Bondeva, P. Tamás, B. Tóth, L. Buday, L. Hunyady, T. Balla, Selective cellular effects of overexpressed pleckstrin-homology domains that recognize PtdIns(3,4,5)P$_3$ suggest their interaction with protein binding partners. *J. Cell Sci.* **118**, 4879–4888 (2005).
49. T. F. Franke, D. R. Kaplan, L. C. Cantley, A. Toker, Direct regulation of the Akt proto-oncogene product by phosphatidylinositol-3,4-bisphosphate. *Science* **275**, 665–668 (1997).
50. S. S. Myatt, E. W. F. Lam, The emerging roles of forkhead box (Fox) proteins in cancer. *Nat. Rev. Cancer* **7**, 847–859 (2007).
51. T. Furuyama, K. Kitayama, Y. Shimoda, M. Ogawa, K. Sone, K. Yoshida-Araki, H. Hisatsune, S. I. Nishikawa, K. Nakayama, K. Nakayama, K. Ikeda, N. Motoyama, N. Mori, Abnormal angiogenesis in Foxo1 (Fkhr)-deficient mice. *J. Biol. Chem.* **279**, 34741–34749 (2004).
52. T. Hosaka, W. H. Biggs III, D. Tieu, A. D. Boyer, N. M. Varki, W. K. Cavenee, K. C. Arden, Disruption of forkhead transcription factor (FOXO) family members in mice reveals their functional diversification. *Proc. Natl. Acad. Sci. U.S.A.* **101**, 2975–2980 (2004).
53. A. Sengupta, S. Chakraborty, J. Paik, K. E. Yutzey, H. J. Evans-Anderson, FoxO1 is required in endothelial but not myocardial cell lineages during cardiovascular development. *Dev. Dyn.* **241**, 803–813 (2012).
54. K. Wilhelm, K. Happel, G. Eelen, S. Schoors, M. F. Oellerich, R. Lim, B. Zimmermann, I. M. Aspalter, C. A. Franco, T. Boettger, T. Braun, M. Fruttiger, K. Rajewsky, C. Keller, J. C. Brüning, H. Gerhardt, P. Carmeliet, M. Potente, FOXO1 couples metabolic activity and growth state in the vascular endothelium. *Nature* **529**, 216–220 (2016).
55. L. T. H. Dang, T. Aburatani, G. A. Marsh, B. G. Johnson, S. Alimperti, C. J. Yoon, A. Huang, S. Szak, N. Nakagawa, I. Gomez, S. Ren, S. K. Read, C. Sparages, A. C. Aplin, R. F. Nicosia, C. Chen, G. Ligresti, J. S. Duffield, Hyperactive FOXO1 results in lack of tip stalk identity and deficient microvascular regeneration during kidney injury. *Biomaterials* **141**, 314–329 (2017).
56. Y. H. Kim, J. Choi, M. J. Yang, S. P. Hong, C.-k. Lee, Y. Kubota, D.-S. Lim, G. Y. Koh, A MST1–FOXO1 cascade establishes endothelial tip cell polarity and facilitates sprouting angiogenesis. *Nat. Commun.* **10**, 838 (2019).
57. S. Choi, A. C. Hedman, S. Sayedyahossein, N. Thapa, D. B. Sacks, R. A. Anderson, Agonist-stimulated phosphatidylinositol-3,4,5-trisphosphate generation by scaffolded phosphoinositide kinases. *Nat. Cell Biol.* **18**, 1324–1335 (2016).
58. N. Thapa, S. Choi, X. Tan, T. Wise, R. A. Anderson, Phosphatidylinositol phosphate 5-kinase Iγ and phosphoinositide 3-kinase/Akt signaling couple to promote oncogenic growth. *J. Biol. Chem.* **290**, 18843–18854 (2015).
59. W. S. Chen, P.-Z. Xu, K. Gottlob, M.-L. Chen, K. Sokol, T. Shiyanova, I. Roninson, W. Weng, R. Suzuki, K. Tobe, T. Kadowaki, N. Hay, Growth retardation and increased apoptosis in mice with homozygous disruption of the akt1 gene. *Genes Dev.* **15**, 2203–2208 (2001).
60. M. Corada, D. Nyqvist, F. Orsenigo, A. Caprini, C. Giampietro, M. M. Taketo, M. L. Iruela-Arispe, R. H. Adams, E. Dejana, The Wnt/beta-catenin pathway modulates vascular remodeling and specification by upregulating Dll4/Notch signaling. *Dev. Cell* **18**, 938–949 (2010).
61. H. Hayashi, T. Kume, Foxc transcription factors directly regulate Dll4 and hey2 expression by interacting with the VEGF-notch signaling pathways in endothelial cells. *PLOS ONE* **3**, e2401 (2008).
62. N. Sacilotto, R. Monteiro, M. Fritzsche, P. W. Becker, L. Sanchez-del-Campo, K. Liu, P. Pinheiro, I. Ratnayaka, B. Davies, C. R. Goding, R. Patient, G. Bou-Gharios, S. de Val, Analysis of Dll4 regulation reveals a combinatorial role for Sox and Notch in arterial development. *Proc. Natl. Acad. Sci. U.S.A.* **110**, 11893–11898 (2013).
63. J. Wythe, L. T. H. Dang, W. P. Devine, E. Boudreau, S. T. Artap, D. He, W. Schachterle, D. Y. R. Stainier, P. Oettgen, B. L. Black, B. G. Bruneau, J. E. Fish, ETS factors regulate Vegf-dependent arterial specification. *Dev. Cell* **26**, 45–58 (2013).
64. G. Bazzoni, E. Dejana, Endothelial cell-to-cell junctions: Molecular organization and role in vascular homeostasis. *Physiol. Rev.* **84**, 869–901 (2004).
65. M. Schramp, N. Thapa, J. Heck, R. Anderson, PIPKIγ regulates β-catenin transcriptional activity downstream of growth factor receptor signaling. *Cancer Res.* **71**, 1282–1291 (2011).
66. A. V. Shah, G. M. Birdsey, C. Peghaire, M. E. Pitulescu, N. P. Dufton, Y. Yang, I. Weinberg, L. Osuna Almagro, L. Payne, J. C. Mason, H. Gerhardt, R. H. Adams, A. M. Randi, The endothelial transcription factor ERG mediates Angiopoietin-1-dependent control of Notch signalling and vascular stability. *Nat. Commun.* **8**, 16002 (2017).
67. J. Zhang, S. Fukuhara, K. Sako, T. Takenouchi, H. Kitani, T. Kume, G. Y. Koh, N. Mochizuki, Angiopoietin-1/Tie2 signal augments basal notch signal controlling vascular quiescence by inducing delta-like 4 expression through AKT-mediated activation of β-catenin. *J. Biol. Chem.* **286**, 8055–8066 (2011).
68. K. Yamamizu, T. Matsunaga, H. Uosaki, H. Fukushima, S. Katayama, M. Hiraoka-Kanie, K. Mitani, J. K. Yamashita, Convergence of Notch and β-catenin signaling induces arterial fate in vascular progenitors. *J. Cell Biol.* **189**, 325–338 (2010).
69. A. Cattelino, S. Liebner, R. Gallini, A. Zanetti, G. Balconi, A. Corsi, P. Bianco, H. Wolburg, R. Moore, B. Oreda, R. Kemler, E. Dejana, The conditional inactivation of the β-catenin gene in endothelial cells causes a defective vascular pattern and increased vascular fragility. *J. Cell Biol.* **162**, 1111–1122 (2003).
70. A. Martowicz, M. Trusohamn, N. Jensen, J. Wisniewska-Kruk, M. Corada, F. C. Ning, J. Kele, E. Dejana, D. Nyqvist, Endothelial β-catenin signaling supports postnatal brain and retinal angiogenesis by promoting sprouting, tip cell formation, and VEGFR (vascular endothelial growth factor receptor) 2 expression. *Atertio. Thromb. Vasc. Biol.* **39**, 2273–2288 (2019).
71. B. T. MacDonald, K. Tamai, X. He, Wnt/β-catenin signaling: Components, mechanisms, and diseases. *Dev. Cell* **17**, 9–26 (2009).
72. A. R. Hernández, A. M. Klein, M. W. Kirschner, Kinetic responses of β-catenin specify the sites of Wnt control. *Science* **338**, 1337–1340 (2012).
73. C. Desbois-Mouthon, A. Cadoret, M. J. Blivet-van Eggelpoël, F. Bertrand, G. Cherqui, C. Perret, J. Capeau, Insulin and IGF-1 stimulate the β-catenin pathway through two signalling cascades involving GSK-3β inhibition and Ras activation. *Oncogene* **20**, 252–259 (2001).
74. S. S. Ng, T. Mahmoudi, E. Danenberg, I. Bejaoui, W. de Lau, H. C. Korswagen, M. Schutte, H. Clevers, Phosphatidylinositol 3-kinase signaling does not activate the Wnt cascade. *J. Biol. Chem.* **284**, 35308–35313 (2009).
75. E. J. McManus, K. Sakamoto, L. J. Armit, L. Ronaldson, N. Shpiro, R. Marquez, D. R. Alessi, Role that phosphorylation of GSK3 plays in insulin and Wnt signalling defined by knockin analysis. *EMBO J.* **24**, 1571–1583 (2005).
76. V. W. Ding, R.-H. Chen, F. McCormick, Differential regulation of glycogen synthase kinase 3β by insulin and Wnt signaling. *J. Biol. Chem.* **275**, 32475–32481 (2000).

77. P. Carmeliet, M. G. Lampugnani, L. Moons, F. Breviario, V. Compernolle, F. Bono, G. Balconi, R. Spagnuolo, B. Oosthuyse, M. Dewerchin, A. Zanetti, A. Angellilo, V. Mattot, D. Nuyens, E. Lutgens, F. Clotman, M. C. de Ruiter, A. Gittenberger-de Groot, R. Poelmann, F. Lupu, J. M. Herbert, D. Collen, E. Dejana, Targeted deficiency or cytosolic truncation of the VE-cadherin gene in mice impairs VEGF-mediated endothelial survival and angiogenesis. *Cell* **98**, 147–157 (1999).
78. S. Gory-Fauré, M. H. Prandini, H. Pointu, V. Roullot, I. Pignot-Paintrand, M. Vernet, P. Huber, Role of vascular endothelial-cadherin in vascular morphogenesis. *Development* **126**, 2093–2102 (1999).
79. K. Gaengel, C. Niaudet, K. Hagikura, B. Laviña, L. Muhl, J. J. Hofmann, L. Ebarasi, S. Nyström, S. Rymo, L. L. Chen, M.-F. Pang, Y. Jin, E. Raschperger, P. Roswall, D. Schulte, R. Benedito, J. Larsson, M. Hellström, J. Fuxe, P. Uhlén, R. Adams, L. Jakobsson, A. Majumdar, D. Vestweber, A. Uv, C. Betsholtz, The sphingosine-1-phosphate receptor S1PR1 restricts sprouting angiogenesis by regulating the interplay between VE-cadherin and VEGFR2. *Dev. Cell* **23**, 587–599 (2012).
80. K. Bentley, C. A. Franco, A. Philippides, R. Blanco, M. Dierkes, V. Gebala, F. Stanchi, M. Jones, I. M. Aspalter, G. Cagna, S. Weström, L. Claesson-Welsh, D. Vestweber, H. Gerhardt, The role of differential VE-cadherin dynamics in cell rearrangement during angiogenesis. *Nat. Cell Biol.* **16**, 309–321 (2014).
81. W. J. Polacheck, M. L. Kutys, J. Yang, J. Eyckmans, Y. Wu, H. Vasavada, K. K. Hirschi, C. S. Chen, A non-canonical Notch complex regulates adherens junctions and vascular barrier function. *Nature* **552**, 258–262 (2017).
82. J. Cao, M. Ehling, S. März, J. Seebach, K. Tarbashevich, T. Sixta, M. E. Pitulescu, A. C. Werner, B. Flach, E. Montanez, E. Raz, R. H. Adams, H. Schnittler, Polarized actin and VE-cadherin dynamics regulate junctional remodelling and cell migration during sprouting angiogenesis. *Nat. Commun.* **8**, 2210 (2017).
83. M. Cavey, T. Lecuit, Molecular bases of cell-cell junctions stability and dynamics. *Cold Spring Harb. Perspect. Biol.* **1**, a002998 (2009).
84. Y. Kam, V. Quaranta, Cadherin-bound β-catenin feeds into the Wnt pathway upon adherens junctions dissociation: Evidence for an intersection between β-catenin pools. *PLOS ONE* **4**, e4580 (2009).
85. K. Ling, S. F. Bairstow, C. Carbonara, D. A. Turbin, D. G. Huntsman, R. A. Anderson, Type Iγ phosphatidylinositol phosphate kinase modulates adherens junction and E-cadherin trafficking via a direct interaction with μ1B adaptin. *J. Cell Biol.* **176**, 343–353 (2007).
86. K. Xiao, D. F. Allison, M. D. Kottke, S. Summers, G. P. Sorescu, V. Faundez, A. P. Kowalczyk, Mechanisms of VE-cadherin processing and degradation in microvascular endothelial cells*. *J. Biol. Chem.* **278**, 19199–19208 (2003).
87. S. Arima, K. Nishiyama, T. Ko, Y. Arima, Y. Hakozaki, K. Sugihara, H. Koseki, Y. Uchijima, Y. Kurihara, H. Kurihara, Angiogenic morphogenesis driven by dynamic and heterogeneous collective endothelial cell movement. *Development* **138**, 4763–4776 (2011).
88. A. Soler, H. Serra, W. Pearce, A. Angulo, J. Guillermet-Guibert, L. S. Friedman, F. Viñals, H. Gerhardt, O. Casanovas, M. Graupera, B. Vanhaesebroeck, Inhibition of the p110α isoform of PI 3-kinase stimulates nonfunctional tumor angiogenesis. *J. Exp. Med.* **210**, 1937–1945 (2013).
89. J. Wüstehube, A. Bartol, S. S. Liebler, R. Brütsch, Y. Zhu, U. Felbor, U. Sure, H. G. Augustin, A. Fischer, Cerebral cavernous malformation protein CCM1 inhibits sprouting angiogenesis by activating DELTA-NOTCH signaling. *Proc. Natl. Acad. Sci. U.S.A.* **107**, 12640–12645 (2010).
90. H. Wang, C. Lin, J. Yao, H. Shi, C. Zhang, Q. Wei, Y. Lu, Z. Chen, G. Xing, X. Cao, Deletion of OSBPL2 in auditory cells increases cholesterol biosynthesis and drives reactive oxygen species production by inhibiting AMPK activity. *Cell Death Dis.* **10**, 627 (2019).
91. I. Egaña, H. Kaito, A. Nitzsche, L. Becker, C. Ballester-Lopez, C. Niaudet, M. Petkova, W. Liu, M. Vanlandewijck, A. Vernaleken, T. Klopstock, H. Fuchs, V. Gailus-Durner, M. Hrabe de Angelis, H. Rask-Andersen, H. J. Johansson, J. Lehtiö, L. He, A. Ö. Yildirim, M. Hellström; German Mouse Clinic Consortium, A. Aguilar-Pimentel, M. Ollert, C. Schmidt-Weber, O. Amarie, J. Graw, J. Beckers, L. Garrett, S. M. Hölter, A. Zimprich, W. Wurst, K. Moreth, R. Bekeredjian, F. Neff, J. Calzada-Wack, I. Rácz, A. Zimmer, B. Rathkolb, E. Wolf, J. Rozman, M. Klingenspor, T. Stoeger, O. Eickelberg, I. Treise, D. H. Busch, M. Östereicher, R. Steinkamp, C. Lengger, H. Maier, C. Stoeger, S. Leuchtenberger, Female mice lacking Pald1 exhibit endothelial cell apoptosis and emphysema. *Sci. Rep.* **7**, 15453 (2017).
92. L. T. Krebs, C. Starling, A. V. Chervonsky, T. Gridley, Notch1 activation in mice causes arteriovenous malformations phenocopied by EphrinB2 and EphB4 mutants. *Genesis* **48**, 146–150 (2010).
93. A. Trindade, S. Ram Kumar, J. S. Scehnet, L. Lopes-da-Costa, J. Becker, W. Jiang, R. Liu, P. S. Gill, A. Duarte, Overexpression of delta-like 4 induces arterialization and attenuates vessel formation in developing mouse embryos. *Blood* **112**, 1720–1729 (2008).
94. H. Uyttendaele, J. Ho, J. Rossant, J. Kitajewski, Vascular patterning defects associated with expression of activated Notch4 in embryonic endothelium. *Proc. Natl. Acad. Sci. U.S.A.* **98**, 5643–5648 (2001).
95. M. A. Rudnicki, R. Jaenisch, The MyoD family of transcription factors and skeletal myogenesis. *Bioessays* **17**, 203–209 (1995).
96. Y. Shimizu-Motohashi, A. Asakura, Angiogenesis as a novel therapeutic strategy for Duchenne muscular dystrophy through decreased ischemia and increased satellite cells. *Front. Physiol.* **5**, 50 (2014).
97. R. Gurung, A. Tan, L. M. Ooms, M. McGrath, R. D. Huysmans, A. D. Munday, M. Prescott, J. C. Whisstock, C. A. Mitchell, Identification of a novel domain in two mammalian inositol-polyphosphate 5-phosphatases that mediates membrane ruffle localization: The inositol 5-phosphatase SKIP localizes to the endoplasmic reticulum and translocates to membrane ruffles following epidermal growth factor stimulation. *J. Biol. Chem.* **278**, 11376–11385 (2003).
98. J. Huelsken, R. Vogel, B. Erdmann, G. Cotsarelis, W. Birchmeier, β-Catenin controls hair follicle morphogenesis and stem cell differentiation in the skin. *Cell* **105**, 533–545 (2001).

Acknowledgments

Tie2-Cre and *Cdh5(PAC)-CreERT2* mice were provided by J. Li (Monash University, Australia) and R. Adams (Max Planck Institute), respectively. We thank T. Balla (NIH, Bethesda, MA) and D. Alessi (University of Dundee, Scotland) for providing the GFP-PH/Btk and YFP-PH-TAPP1 constructs, respectively. We also thank T. Takenawa (Kobe University, Japan) for providing the GST-FYVE/Hrs construct. p*TOP*Flash-Luc reporter gene vector and p*FOP*Flash-Luc vector control were provided by H. Clevers (Hubrecht Institute, Utrecht, The Netherlands). We would like to thank the Biochemistry Imaging Facility, Department of Biochemistry and Molecular Biology, Monash University, and the Monash Micro Imaging Technology Research Platform for technical advice with image acquisition and analysis and the Monash Histology Research Platform for tissue preparation. We thank members of the Mitchell laboratory, and T. Tiganis, and A. Papa for critical review of the manuscript. **Funding:** This work was supported by the National Health and Medical Research Council (NH&MRC), Australia, GNT1010368 (C.A.M.). **Author contributions:** Conceptualization: C.A.M., E.M.D., R.G., G.M.M., and Q.S. Methodology: C.A.M., E.M.D., R.G., G.M.M., and Q.S. Investigation: E.M.D., R.G., K.Q.L., K.T.T.R., R.P.H., and Q.S. Visualization: C.A.M., E.M.D., R.G., K.Q.L., K.T.T.R., R.P.H., and Q.S. Supervision: C.A.M., E.M.D., and R.G. Funding acquisition: C.A.M. Project administration: C.A.M., E.M.D., and R.G. Writing (original draft): E.M.D. and C.A.M. Writing (review and editing): E.M.D., R.G., C.A.M., K.Q.L., K.T.T.R., R.P.H., G.M.M., and Q.S. **Competing interests:** The authors declare that they have no competing interests. **Data and materials availability:** All data needed to evaluate the conclusions in the paper are present in paper and/or the Supplementary Materials. The unique constructs and genetically modified mice generated by this study can be provided by the senior author, C.A.M., pending scientific review and a completed material transfer agreement. Requests should be submitted to christina.mitchell@monash.edu

Submitted 28 June 2022
Accepted 24 February 2023
Published 31 March 2023
10.1126/sciadv.add6911